UAB
Universitat Autònoma
de Barcelona

**Dipòsit digital
de documents
de la UAB**

Metal-oxide Clusters on Nitrogen-doped Carbon are highly Selective for CO_2 Electroreduction to CO

Jingkun Li[1], Andrea Zitolo[2], Felipe A. Garcés-Pineda[3], Tristan Asset[4], Mounika Kodali[4], PengYi Tang[5], Jordi Arbiol,[5,6] José Ramón Galán-Mascarós[3,6], Plamen Atanassov[4], Iryna V. Zenyuk[4], Moulay Tahar Sougrati[1], and Frédéric Jaouen[1]*

1 ICGM, Univ. Montpellier, CNRS, ENSCM, 34090 Montpellier, France

2 Synchrotron SOLEIL, L'orme des Merisiers, BP 48 Saint Aubin, 91192 Gif-sur-Yvette, France

3 Institute of Chemical Research of Catalonia, ICIQ, The Barcelona Institute of Science and Technology, Av. Països Catalans, 16, 43007 Tarragona, Spain

4 Department of Chemical and Biomolecular Engineering, National Fuel Cell Research Center, University of California Irvine, Irvine, 92697, United States

5 Catalan Institute of Nanoscience and Nanotechnology (ICN2), CSIC and BIST, Campus UAB, Bellaterra, 08193 Barcelona, Catalonia, Spain

6 ICREA, Pg. Lluís Companys 23, 08010 Barcelona, Catalonia, Spain

* Corresponding author: Frédéric Jaouen (frederic.jaouen@umontpellier.fr)

1

Abstract

The electrochemical reduction of CO_2 (eCO$_2$RR) using renewable energy is an effective approach to pursue carbon neutrality. The eCO$_2$RR to CO is indispensable to promoting C-C coupling through bifunctional catalysis and to achieving cascade conversion from CO_2 to C_{2+}. This work investigates a series of M/N-C (M=Mn, Fe, Co, Ni, Cu and Zn) catalysts for which the metal precursor interacted with the nitrogen-doped carbon support (N-C) at room temperature, resulting in the metal being present as (sub)nano-sized metal oxide clusters in *ex situ* condition, except for Cu/N-C and Zn/N-C. A volcano trend in their activity toward CO as a function of the group of the transition metal is revealed, with Co/N-C exhibiting the highest activity at -0.5 V *vs.* RHE; while Ni/N-C shows both appreciable activity and selectivity. *Operando* XAS shows that the majority of Cu atoms in Cu/N-C forms Cu^0 clusters during eCO$_2$RR; while the Mn/, Fe/, Co/, and Ni/N-C maintain the metal hydroxide structures, with a minor amount of M^0 formed in Fe/, Co/, and Ni/N-C. The superior activity of Fe/, Co/ and Ni/N-C is ascribed to the phase contraction and the HCO_3^- insertion into the layered structure of metal hydroxides. Our work provides a facile synthetic approach toward highly active and selective electrocatalysts to convert CO_2 into CO. Coupling with state-of-the-art NiFe-based anodes in a full cell device, Ni/N-C exhibits >80% Faradaic efficiency toward CO at 100 mA cm^{-2}.

Keywords: CO_2 electroreduction, metal oxide clusters, volcano trend, *operando* X-ray absorption spectroscopy, phase contraction, nitrogen-doped carbon

1. Introduction

The direct electrochemical CO_2 reduction reaction (eCO$_2$RR) to fuels and valuable chemicals, powered by renewable energies, is an attractive pathway to establish a carbon-neutral energy cycle. However, the implementation of CO_2 electrolyzers is still impeded by: 1) low energy efficiency due to the high overpotential needed to activate CO_2;[1] 2) low Faradaic efficiency (FE) due to competing hydrogen evolution reaction (HER) in aqueous electrolytes;[1] 3) low current densities due to poor CO_2 mass transport when using CO_2-saturated aqueous electrolytes as cathode feed.[2, 3] In the past decades, research in the field of eCO$_2$RR has focused on developing efficient and selective electrocatalysts *via* surface functionalization,[4, 5] metal alloying,[6, 7] heteroatom doping,[8] facet/morphology regulation,[9, 10] and particle size tailoring[11]. Recently, industrial scale current densities (>100 mA·cm^{-2}) have been achieved *via* enhanced mass transport of CO_2 in gas-diffusion electrodes (GDEs).[12-16]

Depending on the nature of catalytic sites and the operating conditions, C_1 (CO, CH_4, CH_3OH, HCOOH, *etc.*), C_2 (C_2H_4, CH_3CH_2OH, CH_3COOH, *etc.*) and C_3 (n-C_3H_7OH, *etc.*) products have been reported for eCO$_2$RR.[1] The state-of-the-art Faradaic efficiency (FE) of eCO$_2$RR to C_1 products (CO or formate) is >90% over Zn,[17] Ag,[18] Au,[19] SnO_x[20] and catalysts comprising single-metal-atom sites.[21-25] However, only Cu-based catalysts promote the production of C_{2+} chemicals but, hitherto, with low FEs (<50%) toward a particular C_{2+} product.[6, 8-10] Only few studies have, to the best of our knowledge, reported the reduction of CO_2 toward a C_2 product (acetic acid) over Cu-free catalysts and with significant selectivity.[26-28] To date, the most efficient approach to favour C_{2+} products *vs*. CO, CH_4 and formic acid is the fine tuning of the surface structure of Cu, including the oxidation state, defects, crystal facets and doping with a secondary metal.[6, 8-10, 29-32] The doping of Cu with Ag, Au and Zn leans, partially, on the high selectivity for CO_2-to-CO of such metallic surfaces and the

3

recognized importance of the CO intermediate in the formation of C_2 products on Cu.[33-37]. Doping Cu with Ag, Au and Zn can thus be described as introducing bifunctionality at the atomic scale. However, the extent to which Cu can be doped by CO-selective sites is limited,[35, 36] and the doping simultaneously alters the geometric and electronic structures of the Cu surface, modifying its selectivity.[6, 38-41] In addition, such advanced surface structures prepared and optimized *ex situ* generally experience significant reconstructions during eCO$_2$RR, either due to the low electrochemical potential and/or due to *operando* produced CO.[42-44]

Recently, alternative bifunctional catalysis approaches have been investigated in which CO is produced on one type of active sites and subsequently desorbed and transported to other sites that catalyse C-C coupling.[4, 5, 36, 45] Compared to atomic-level bifunctionality, this approach disentangles the effect of the two catalytic sites and allows optimizing them separately. For example, E.H. Sargent's group *et al.* [36] demonstrated that metallic copper/metal-porphyrin composite cathodes promote the C-C coupling, leading to higher peak Faradaic efficiency (FE) of 41% toward ethanol compared to that of 29% over pure Cu. Similarly, P. Strasser's group reported that the ethylene production rate was 3-fold faster on Cu nanoparticles mixed with Ni-N-C than on Cu nanoparticles alone.[45]

These examples show that CO-making sites do not need to be at atomic distance of the Cu surface in order to enhance Cu selectivity towards C_2 products. This opens the door to diverse strategies at the cathode, electrolyzer and system levels in order to tune the product selectivity. For example, CO/CO$_2$ feed was shown to increase the selectivity towards ethylene compared to pure CO$_2$ feed.[45] The eCO$_2$RR towards multi-carbon products might thus be achieved in two stages from a cell engineering viewpoint as well, for example with a first electrolyzer cell with a cathode designed to produce syngas from CO$_2$, and the syngas serving as inlet gas for a second electrolyzer cell where a Cu-based cathode transforms it selectively into C_2 products.[46]

In addition, complete electrochemical conversion of CO_2-to-CO in the first stage would be beneficial as it would allow carrying out electrochemical reduction of CO to C_{2+} products at high pH (13-14) in the second stage, with more facile kinetics than in near-neutral pH.[2, 47] In contrast, sustainably operating eCO_2RR at high pH is impossible, due to the fast carbonation of high-pH catholyte with CO_2-gas feed.[2, 3]

Thus, it is of paramount importance to develop a robust, efficient and selective electrocatalyst for eCO_2RR to CO to realize the practical implementation of CO_2 electrolyzers. Metal-nitrogen-carbon (M-N-C, with M=Mn, Fe, Co, Ni, and Cu) materials that exclusively comprise atomically-dispersed MN_x sites have shown high selectivity toward CO (especially for M = Fe or Ni).[21-25] Excessive metal content however leads to aggregation of a fraction of metal during pyrolysis into particles, resulting in lower selectivity towards CO.[48-50] The synthesis of M-N-C catalysts comprising only MN_x sites is therefore not trivial and requires optimisation of the content and nature of the metal, N and C precursors, as well as one or several pyrolysis steps and, often, post-pyrolysis treatment to remove excess metal.[22-24, 51] This has drawback on the life-cycle assessment if such catalysts were implemented in industrial-scale CO_2 electrolyzers. MN_4 macrocycles such as phthalocyanines and porphyrins adsorbed or attached onto carbon allotropes have shown high selectivity for CO formation, comparable to that of M-N-C materials.[52-54] However, the synthesis of such macrocycles is not ideal for large-scale production of low-cost catalyst. Moreover, it has been reported that both MN_x sites (in pyrolyzed M-N-C) and MN_4 sites (in macrocycles supported *e.g.* on carbon) are prone to clustering during eCO_2RR, as observed *via operando* X-ray absorption spectroscopy (XAS).[25, 55, 56] While the Cu clusters formed at low potential re-dispersed into single-Cu-atom sites when scanning the potential up, this observation raises the question whether the fine structure of M-N-C materials with exclusive single-atom MN_x sites is necessary for high CO_2-to-CO selectivity.

5

Herein, we developed and studied a series of M/N-C (M=Mn, Fe, Co, Ni, Cu and Zn) catalysts featuring highly-dispersed metal-oxide particles supported on nitrogen-doped carbon (N-C) under *ex situ* condition, except for Cu/N-C and Zn/N-C, featuring mainly atomically dispersed sites. Their catalytic activity and selectivity toward eCO_2RR to CO was evaluated in a flow cell with GDEs. A volcano trend in their activity toward CO as a function of the group of the transition metal is revealed, with Co/N-C exhibiting the highest intrinsic activity at –0.5 V *vs.* RHE; while Ni/N-C shows both high activity and selectivity. *Operando* XAS was further exploited to investigate structural changes under working conditions. The majority of Cu atoms in Cu/N-C forms Cu^0 clusters during eCO_2RR; while the Mn/, Fe/, Co/, and Ni/N-C maintain the metal hydroxide structures, with a minor amount of M^0 formed *in operando* with Fe/, Co/, and Ni/NC samples. Then the M/N-C cathodes were coupled with state-of-the-art NiFe-based anodes in PGM-free electrolyzer cells, with Ni/N-C exhibiting >80% FE toward CO at 100 mA cm^{-2} at a cell voltage of ~4 V.

2. Results and discussion

2.1. *Ex situ* identification of the metal coordination in M/N-C

The metal coordination and presence of metal-oxide particles supported on N-C, is firstly studied and revealed under *ex situ* condition for the series of materials developed in this work and labelled as M/N-C (M=Mn, Fe, Co, Ni, Cu and Zn). The metal coordination and spectral response is also compared with M-N-C catalysts previously studied at our laboratory, and featuring exclusively atomically dispersed MN_x sites. The synthesis of M-N-C catalysts was described in a previous work.[25] Briefly, the well-mixed precursors of metal acetate, 1,10-phenanthroline and ZIF-8 (Basolite® Z1200) were pyrolyzed in Ar at 1050 °C in flash mode. In contrast, the M/N-C catalysts (M = Mn, Fe, Co, Ni, Cu) were synthesized *via* chemical precipitation wherein the transition metals were deposited on N-C by dissolving $M^{(II)}Cl_2$ salt

6

in a suspension of N-C in water/ethanol (see Experimental Methods for the detailed protocol). The N-C support was prepared *via* pyrolysis of ZIF-8, as described further below. Then the suspension was centrifuged, washed with water and let to dry in ambient conditions. The dry powder was finally subjected to a mild heat treatment at 200°C for 2 h in flowing Ar, for complete drying. The major difference between the synthesis of M-N-C and M/N-C is that the metal atoms were subjected to a high-temperature pyrolysis for the former synthesis, leading to the formation of atomically dispersed $M-N_4$ sites, but not for the latter synthesis. The N-C support was synthesized by pyrolysis of ZIF-8, with a first pyrolysis in flash mode in flowing Ar at 1050°C for 1 h, followed by a second flash pyrolysis in flowing NH_3 at 900°C for 10 min. The second pyrolysis was introduced to increase the N-content and surface basicity. As will be shown later, the presence of nitrogen in the carbon substrate is key to the CO_2RR activity of the present M/N-C materials. It should be noted here that the N-C support contains $Zn-N_4$ sites (**Figure S1**). However, we label it as N-C for simplicity and also because the $Zn-N_4$ sites were previously demonstrated to be inactive towards CO_2RR.[25]

The bulk metal contents in M/N-C materials were derived from the absolute absorption height of XAS spectra, measured in transmission mode and for a fixed catalyst weight per cross section of pellet. They are shown in **Table S1**, with metal loadings varying between 1.3 and 2.5 wt.%. This agrees with the metal contents obtained by X-ray photoelectron spectroscopy (XPS) in the range of 0.5 to 2.2 wt.% (**Table S2**). All M/N-C materials also contain a significant amount of Zn, derived from ZIF-8, that is comparable to the Zn amount in the N-C substrate (**Table S2**). The Zn is present as atomically dispersed ZnN_4 moieties, as shown by X-ray absorption near edge spectroscopy (XANES) and extended X-ray absorption fine structure (EXAFS) (**Figure S1**). The same ZnN_4 site and similar Zn content were also observed after a single pyrolysis in Ar of ZIF-8.[25]

The X-ray diffraction (XRD) patterns of M/N-C materials (**Figure S2**) exhibit only two broad peaks typical for nanometric graphite-like domains present in amorphous N-C, and no diffraction peaks related to metal-based crystalline structures. XRD is however not ideally suited to identify the possible presence of metal clusters in such materials, due to i) the low metal content on N-C (**Tables S1-S2**), ii) the small size of metal clusters, or iii) the amorphous character of metal clusters due to the mild synthesis conditions. To obtain precise information on the metal coordination and oxidation state in M/N-C, we then resorted to ^{57}Fe Mössbauer spectroscopy for Fe/N-C, and XAS at the metal K-edge for all M/N-C.

The Mössbauer spectrum acquired at room temperature shows only one quadrupole doublet (**Figure 1a**), with isomer shift and quadrupole splitting values of 0.31 and 0.81 mm·s^{-1}, respectively (**Table S3**). While this doublet can generally be assigned to Fe^{3+} in high-spin (HS) state,[57] Mössbauer measurement at room temperature cannot distinguish between HS Fe^{3+} in amorphous or (sub)-nanometric Fe_2O_3 and HS Fe^{3+} in atomically-dispersed sites.[58, 59] In the context of this study, Fe sites in Fe/N-C might exist as a result of possible trans-metalation from ZnN_4 moieties (present in N-C) to FeN_4 moieties during the precipitation of Fe onto N-C in aqueous solution,[60, 61] or as a result of Fe^{2+} adsorption on N- or O-functional groups on the surface of N-C, followed by oxidation during the drying step in air.

We then performed ^{57}Fe Mössbauer spectroscopy at 5 K, taking advantage of the different temperature-dependent behaviours of the Mössbauer spectrum of nanometric ferric oxides and atomically-dispersed Fe-sites, the former changing from doublet to sextet signal below a certain critical temperature,[62] while the latter remains a doublet even at 5 K.[59, 63] The 5 K Mössbauer spectrum of Fe/N-C exhibits three sextets with slightly different IS-values and hyperfine fields (HF) amounting to 96 % of the resonant area, as well as a minute amount of a quadrupole doublet (4 %) (**Figure 1b** and **Table S3**). The IS- and HF values of the three sextets

can be assigned to Fe_2O_3 with different particle sizes,[62, 64] while the doublet is assigned to HS

Fe^{2+}, due to its high isomer shift of 1.07 mm·s^{-1}.[65] Thus, the 5 K Mössbauer spectrum

demonstrates that the well-defined narrow doublet observed at room temperature is

overwhelmingly arising from amorphous or (sub)nano-sized Fe_2O_3.
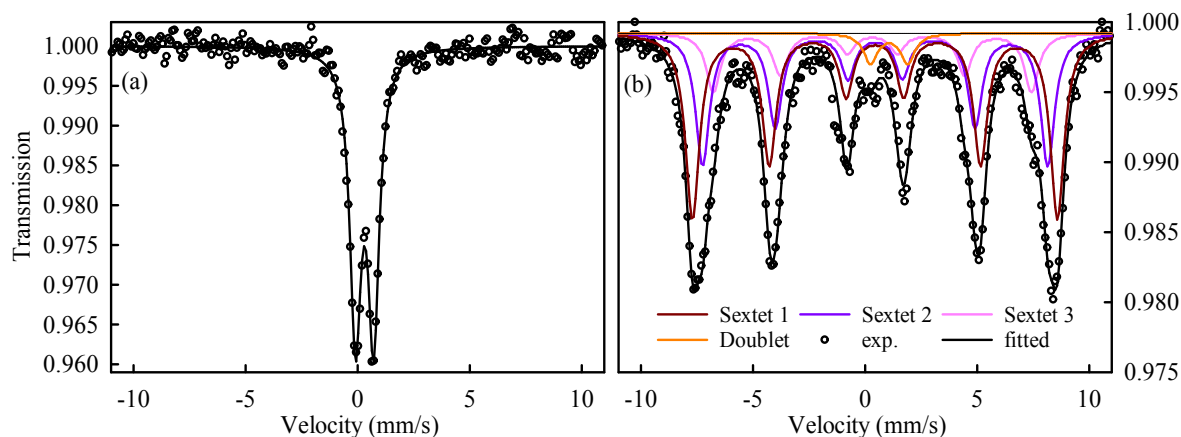
Figure 1. *Ex situ* ^{57}Fe Mössbauer spectra for Fe/N-C measured at room temperature (a) and 5

K (b).

This is also well supported by *ex situ* XAS at the Fe K-edge. The XANES spectrum of Fe/N-

C highly resembles that of a commercial Fe_2O_3 powder as far as the edge position and the main

spectral features are concerned (**Figure S3a**). Moreover, the Fourier transform (FT) of the

EXAFS spectrum of Fe/N-C shows two prominent peaks at ~1.5 and ~2.5 Å (uncorrected for

phase shift), matching the Fe-O and Fe-Fe (labelled Fe-Fe$_{oxy}$) interactions in Fe_2O_3 (**Figure

2a**). Similar to our synthesis for Fe/N-C, R. Arrigo *et al.* deposited iron on a N-functionalized

carbon paper from nitrate salt and identified with XAS the iron species to be

oxides/oxyhydroxides.[26] We also note that the XANES and EXAFS spectra of Fe/N-C are

different from those of a Fe-N-C material from our laboratory, prepared by the direct pyrolysis

of Fe(II) salt, ZIF-8 and phenanthroline, comprising Fe exclusively as atomically-dispersed

FeN$_x$ sites that form at high temperature. The XANES spectra of Fe/N-C and Fe-N-C differ in

shape with a lower white line intensity, scaling with Fe-O interactions, for the latter (**Figure

S3a). The FT-EXAFS spectra of Fe/N-C and Fe-N-C also differ, the latter only shows one major peak at ~1.5 Å due to Fe-N (and Fe-O) interactions from (O_2)-FeN$_x$ moieties,[66, 67] but no peak at 2.5 Å (**Figure 2a**).

To investigate the metal coordination in the other M/N-C catalysts, we performed *ex situ* XAS at their respective metal K-edges and compare spectral features to those of i) reference metal oxide materials and ii) a series of M-N-C materials prepared at high temperature and comprising only atomically-dispersed MN$_x$ sites.[25] The intensity of the white line of Co/N-C XANES is consistent with that of the oxides, and the position of the edge is close to that of Co$_2$O$_3$ (**Figure S3b**). The Ni/N-C XANES spectrum matches well the reference NiO spectrum over a broad energy range (**Figure S3c**). Moreover, the position of the absorption edges indicates that the average oxidation state of Ni in Ni/N-C is close to that of Ni in NiO (Ni^{2+}). The main peak in the FT-EXAFS spectra of Co/N-C at ~1.4 Å matches well the position of the Co-O backscattering signal in Co$_3$O$_4$ while the second peak at ~2.3 Å matches the position of the Co-Co$_{oxy}$ backscattering signal in Co$_3$O$_4$ and/or CoO (**Figure 2b**). This is even clearer for Ni/N-C, with the positions of the two main peaks in its FT-EXAFS spectrum at ~1.5 and ~2.6 Å matching perfectly those for the Ni-O and Ni-Ni$_{oxy}$ backscattering paths of NiO (**Figure 2c**). Similarly as for Fe/N-C, the XANES and FT-EXAFS spectra of Co/N-C and Ni/N-C differ from the corresponding spectra of Co-N-C and Ni-N-C materials from our laboratory, that comprise only single-metal-atom MN$_4$ moieties.[25] In the FT-EXAFS, the Co-N-C and Ni-N-C reference materials show only one peak with slightly lower bond distance compared to the main peak in M/N-C materials (1.3 *vs.* 1.4–1.5 Å), assigned to M-N bonds (**Figure 2b-c**, compare red and blue curves). In the XANES spectra, the intensity of the white-line peak is much weaker for Co-N-C and Ni-N-C compared to Co/N-C and Ni/N-C, respectively, indicating a lower fraction of M-O bonds (**Figure S3b-c**, compare red and blue curves). In

10

summary, the *ex situ* XAS spectra of Co/N-C and Ni/N-C demonstrate that the majority of transition metals are in the form of amorphous or (sub)nanometric oxides.

Regarding Cu/N-C, its XANES spectrum is dissimilar with those of CuO and Cu_2O but resembles more that of Cu-N-C (**Figure S3d**). Similarly, the FT-EXAFS spectrum of Cu/N-C closely resembles that of Cu-N-C, with a single peak at ~1.4 Å and no secondary peak at the position expected for $Cu-Cu_{oxy}$ backscattering (**Figure 2d**). This suggests that Cu might be atomically dispersed as CuO_x or CuN_x sites. The latter label does however not necessarily imply the exact same coordination as Cu in Cu-N-C (CuN_4, formed at high temperature), and we stress that the XANES spectra of Cu/N-C and Cu-N-C are slightly different (**Figure S3d**). Transmetalation between ZnN_x and Cu^{2+} in solution, forming CuN_x sites, may be more facile than with Fe^{2+}, Co^{2+} or Ni^{2+} cations in solution due to steric or electronic effects, as reported for metalation/transmetalation of metal-free porphyrins.[68]
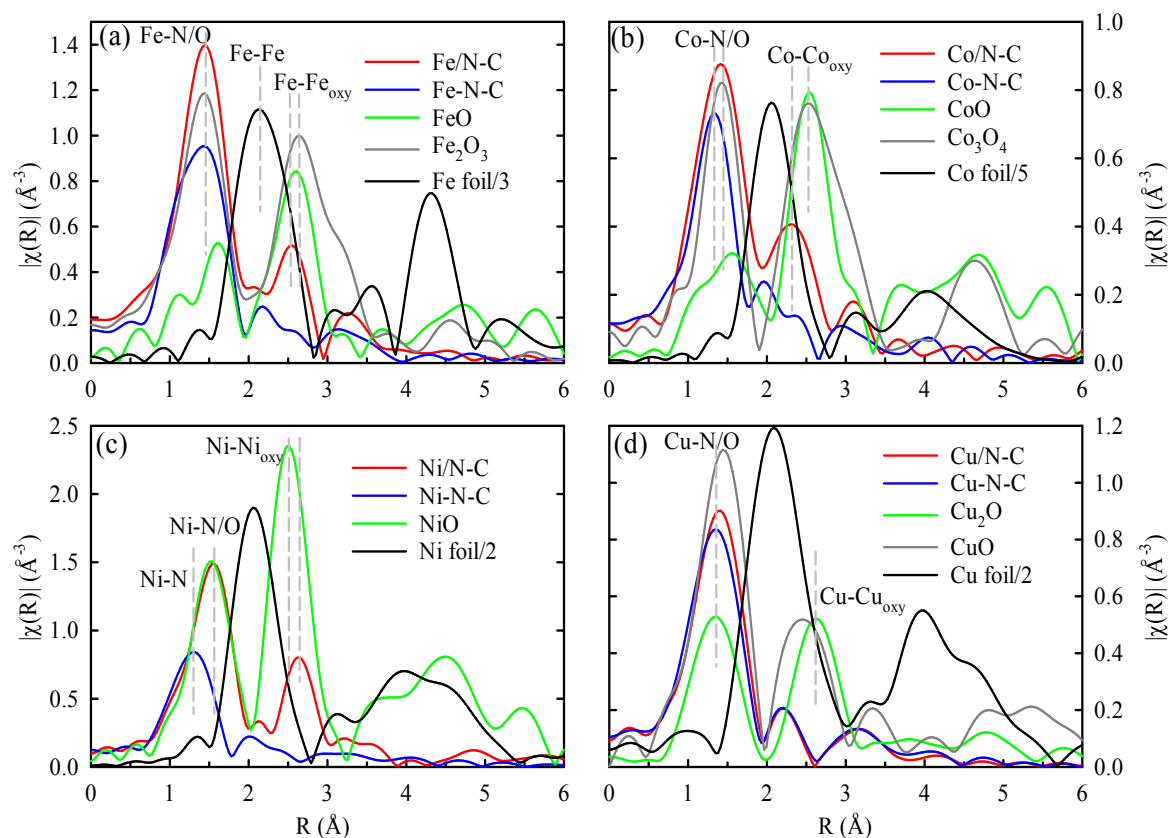
Figure 2. Non phase-shift corrected *ex situ* FT-EXAFS spectra of Fe/N-C (a), Co/N-C (b), Ni/N-C (c) and Cu/N-C (d). For each metal, the FT-EXAFS spectra for metallic foils, metal oxide powders and M-N-C powder catalysts with MN_4 moieties are also presented as references.

To further study the morphologies of the metal-rich clusters in this series of M/N-C catalysts, we then resorted to aberration-corrected scanning transmission electron microscopy (STEM). Metal-rich nanoparticles with irregular shapes are identified in Fe/, Co/ and Ni/N-C samples (**Figure 3a**, **c**, **e**), in line with the $M-M_{oxy}$ interactions detected in EXAFS; whereas areas without any obvious clusters/nanoparticles are also observed (**Figure 3b**, **d**, **f**, **h**). Notably, Cu/N-C shows very few metal-rich clusters even after an extensive investigation on multiple areas (**Figure 3g**), explaining the absence of $Cu-Cu_{oxy}$ interaction in the FT-EXAFS spectra (**Figure 2d**). Moreover, single-metal-atoms are clearly seen in M/N-C (**Figure S4**); however, we cannot conclusively say they are Co, Ni or Cu single-atom-sites, since the N-C support contains a non-negligible amount of atomically dispersed ZnN_4 moieties (**Figure S1**), and the HAADF STEM cannot distinguish Zn from other metals. In summary, the transition metals in M/N-C are present mainly as clusters of oxides, except for the case of Cu/N-C with CuN_x or CuO_x moieties formed *via* transmetalation or adsorption.
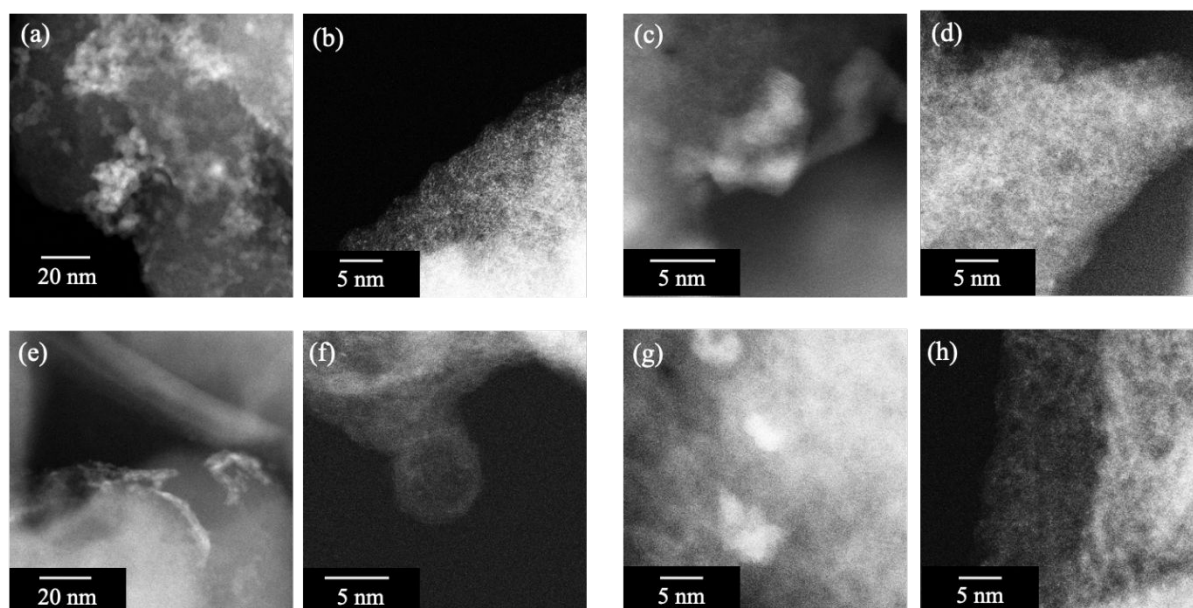
Figure 3. HAADF STEM images of Fe/N-C (a, b), Co/N-C (c, d), Ni/N-C (e, f) and Cu/N-C (g, h).

The nitrogen speciation of the M/N-C catalysts was then investigated with XPS. The N1s narrow-scan spectra were deconvoluted into five nitrogen species, namely pyridinic nitrogen, amine or N in MN_x, pyrrolic N (labelled N-H), graphitic N (including N_{gr}/N^+ and bulk N-H, *i.e.* N-H in the carbon plane) and N-O_x (**Figure S5**). The nitrogen chemistry of M/N-C catalysts resembles that of the N-C substrate, with similar relative concentrations of different N species, including in particular 15.8–18.9 relative % of N as "MN_x" (**Table S2**).

As for the EXAFS and XANES data, we find it useful to compare the XPS N1s narrow-scan spectra of M/N-C materials to those for M-N-C. Since the N1s spectra for M-N-C are also similar for different 3d metals,[25] we show and discuss the N1s spectrum of Fe-N-C only as a representative example. The N1s spectrum of Fe-N-C was fitted with the same N-species (**Figure S5f**) but contains different relative concentrations of N-species compared to M/N-C (**Table S2**). Specifically, the ratios of N-Pyridinic to MN_x are 1.9–2.3 for M/N-C materials and the N-C substrate as well, but only ~1.6 for Fe-N-C. The latter might indicate that pyridinic N

13

are preferentially utilized for forming FeN_x sites during pyrolysis in the presence of Fe. In contrast, similar N-Pyridinic/M-N_x ratios for all M/N-C materials and for the N-C substrate suggests that pyridinic nitrogen did not bind metal cations during the metal salt precipitation, and that the MN_x signal in M/N-C can mainly be assigned to ZnN_x sites that were already present in the N-C substrate. Transmetalation of a fraction of ZnN_x sites into CuN_x sites would also lead to a ratio of N-Pyridinic/M-N_x similar to that in N-C, and the XPS results are thus not contradicting the XANES and EXAFS conclusions on Cu/N-C.

We also synthesized the Mn/ and Zn/N-C catalysts and their structures were studied with *ex situ* XAS and XRD (**Figure S6**). The peaks at ~1.4, ~2.7 and ~4.8 Å in the FT-EXAFS spectrum of Mn/N-C coincides with the Mn-O and Mn-Mn_{oxy} interactions in manganese oxides, while the additional peak at ~2.1 and 3.3 Å are also indicative of the presence of MnOOH (**Figure S6a**). The remaining presence of a metal hydroxide in Mn/N-C and absence in the other M/N-C samples is due to the significantly higher decomposition temperature of γ-MnOOH (> 300 °C) compared to the metal (oxy)hydroxides for Fe, Co, Ni, Cu and Zn.[69] The XRD pattern of Mn/N-C shows two peaks at ~33° and 36° attributed to Mn_2O_3 and Mn_3O_4, respectively,[70] in addition to the two broad peaks arising from amorphous carbon (**Figure S6c**). These results show that Mn/N-C contains manganese oxides/oxyhydroxides with relatively larger particles sizes compared to other M/N-C, on the basis of their detection by XRD. Regarding Zn/N-C, it contains both ZnN_4 sites (already present in N-C) and zinc species that were formed during the subsequent adsorption/precipitation process. As a result, the XANES and FT-EXAFS of Zn/N-C closely resemble that of N-C, except for a minor peak at ~2.9 Å attributed to Zn-Zn_{oxy} interaction as in ZnO. In contrast to Mn/N-C, the ZnO clusters are not detected by XRD, suggesting amorphous or sub-nanometric ZnO clusters.

In summary, *ex situ* XAS, [57]Fe Mössbauer spectroscopy, XRD and STEM results demonstrate the presence of highly dispersed transition metal oxides (MO_x) supported on N-C (comprising ZnN_x sites) in M/N-C materials, except for Cu/N-C comprising atomically dispersed CuO_x or CuN_x sites, with possible transmetalation from ZnN_x to CuN_x sites.

## 2.2 Activity and selectivity of M/N-C materials for eCO₂RR

To measure the activity and selectivity, we resorted to an electrochemical flow cell with a GDE cathode configuration, with CO_2 gas feed at the back and, in this section, a continuous flow of 1 M $KHCO_3$ as catholyte at the front (hydrophobic side) of the GDE. The anode and anolyte utilized in this section were IrO_x coated Ti plate and 1 M $KHCO_3$, respectively. The Ag/AgCl reference electrode was placed in the catholyte chamber. The gaseous products of eCO₂RR were identified and quantified under galvanostatic control (see details in Experimental Methods). **Figure 4** shows the Faradaic efficiencies (FE) for CO and H_2 for all M/N-C materials as well as for N-C, for different current densities ranging from 2 to 20 mA·cm^{-2}. The sum of the Faradaic efficiencies (FE) for CO and H_2 is ≥ 90 % for all M/N-C materials, indicating no or restricted formation of CO_2RR liquid products. The FEs for CO an H_2 vary strongly both as a function of the nature of the metal in the catalyst and also as a function of the current density (**Figure 4**). The trends of FEs *vs.* current density are shown in **Figure 5a-d** for down-selected materials, namely Fe/, Co/, Ni/ and Cu/N-C. In contrast to Fe/ and Cu/N-C with a bell shape in FE *vs.* current density (CO selectivity first increases with current density, reaches a maximum and then decreases at even higher current density), Co/N-C and Ni/N-C show increasing CO selectivity with current density up to 20 mA·cm^{-2} (**Figure 5a-d**). The maximum selectivity towards CO is reached at 5 mA·cm^{-2} for Fe/N-C (*ca* 70 % CO) and Cu/N-C (ca 50% CO) (**Figure 5a** and **5d**), while the CO selectivity over Co/ and Ni/N-C reaches 73 and 90% at 20 mA·cm^{-2}, respectively (**Figure 5b-c**).

Figure 5e shows the CO partial current density (J_{CO}) *vs*. cathode potential for all M/N-C materials and for N-C as well. All M/N-C catalysts show an earlier onset for eCO$_2$RR to CO than the N-C substrate, demonstrating the catalytic role of the metal species added to the N-C substrate (itself containing ZnN$_x$ sites). Co/N-C shows the highest onset potential, > -0.3 V *vs*. RHE, *i.e.* an absolute overpotential < 200 mV for eCO$_2$RR to CO (E^o = -0.104 V *vs*. RHE[1]). This onset potential is comparable to those reported for precious metal-based catalysts toward eCO$_2$RR to CO at similar pH.[19, 71, 72] The Fe/ and Ni/N-C materials have the second highest onset potential, but while the polarization curves are almost overlapped at low current density (< 2.5 mA·cm^{-2}), they split at high current density with the Ni/N-C polarization curve showing an exponential growth with decreasing cathode potential while the one for Fe/N-C shows a nearly linear increase down to *ca* -0.55 V *vs*. RHE (**Figure 5e**). This is due to the sharp decrease in FE(CO) for Fe/N-C at a total current density > 5 mA·cm^{-2} (**Figure 5a**), while the FE(CO) of Ni/N-C continuously increases with increasing total current density (**Figure 5c**). The J_{CO} polarization curves of the Mn/N-C, Cu/N-C and Zn/N-C catalysts are similar and much lower than those of Fe/N-C, Co/N-C and Ni/N-C (**Figure 5e**), due mostly to low FE(CO) on those materials at current densities > 5 mA·cm^{-2} (**Figure 4c-d**). In summary, these flow cell measurements identify the Co- and Ni/N-C as the most promising catalysts in this series for electrochemical CO production at high current densities.
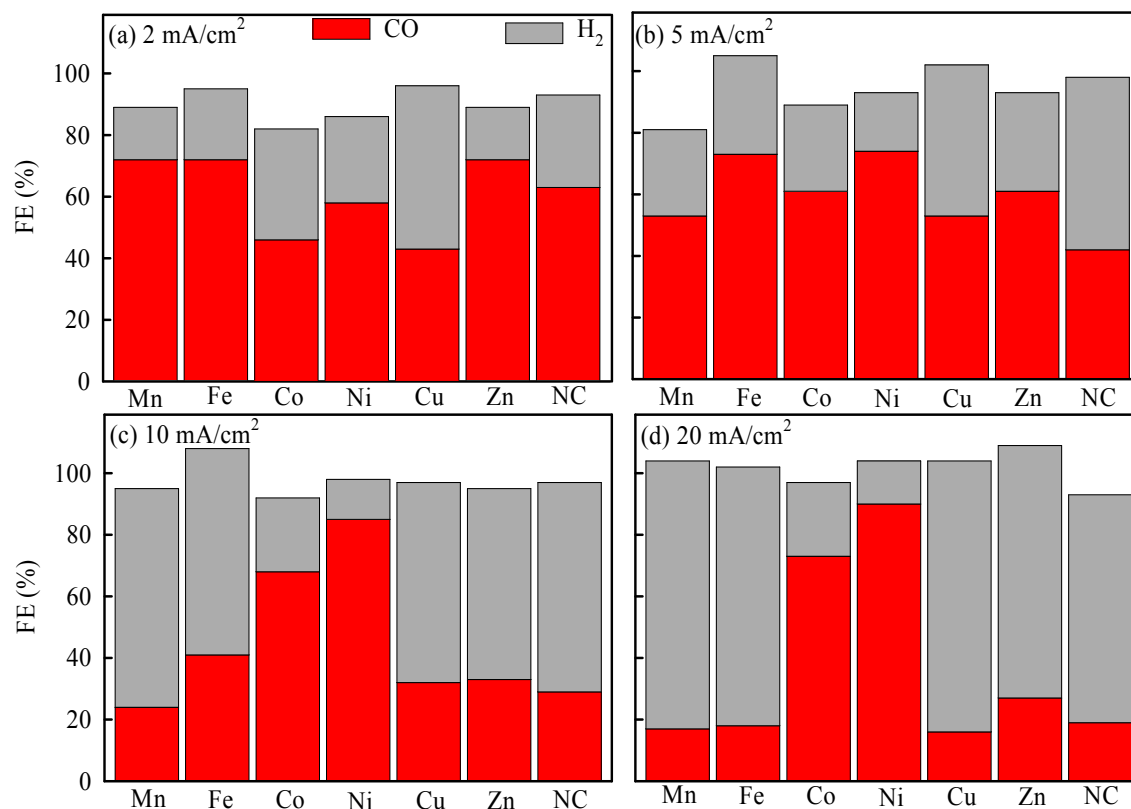
Figure 4. The FEs at different current densities over M/N-C catalysts (M = Mn, Fe, Co, Ni, Cu

and Zn) at 2 (a), 5 (b), 10 (c) and 20 (d) $mA \cdot cm^2$. The measurements were performed in flow

cell under galvanostatic control for ~90 min in 1 M $KHCO_3$ aqueous catholyte and anolyte at

room temperature, CO_2 gas was fed at 50 mL min^{-1} at the back of the GDE. The cathode

catalyst loading was 1 $mg \cdot cm^{-2}$, the membrane was Tokuyama Neosepta® anion exchange

membrane, and the anode was a flat IrO_x electrode.
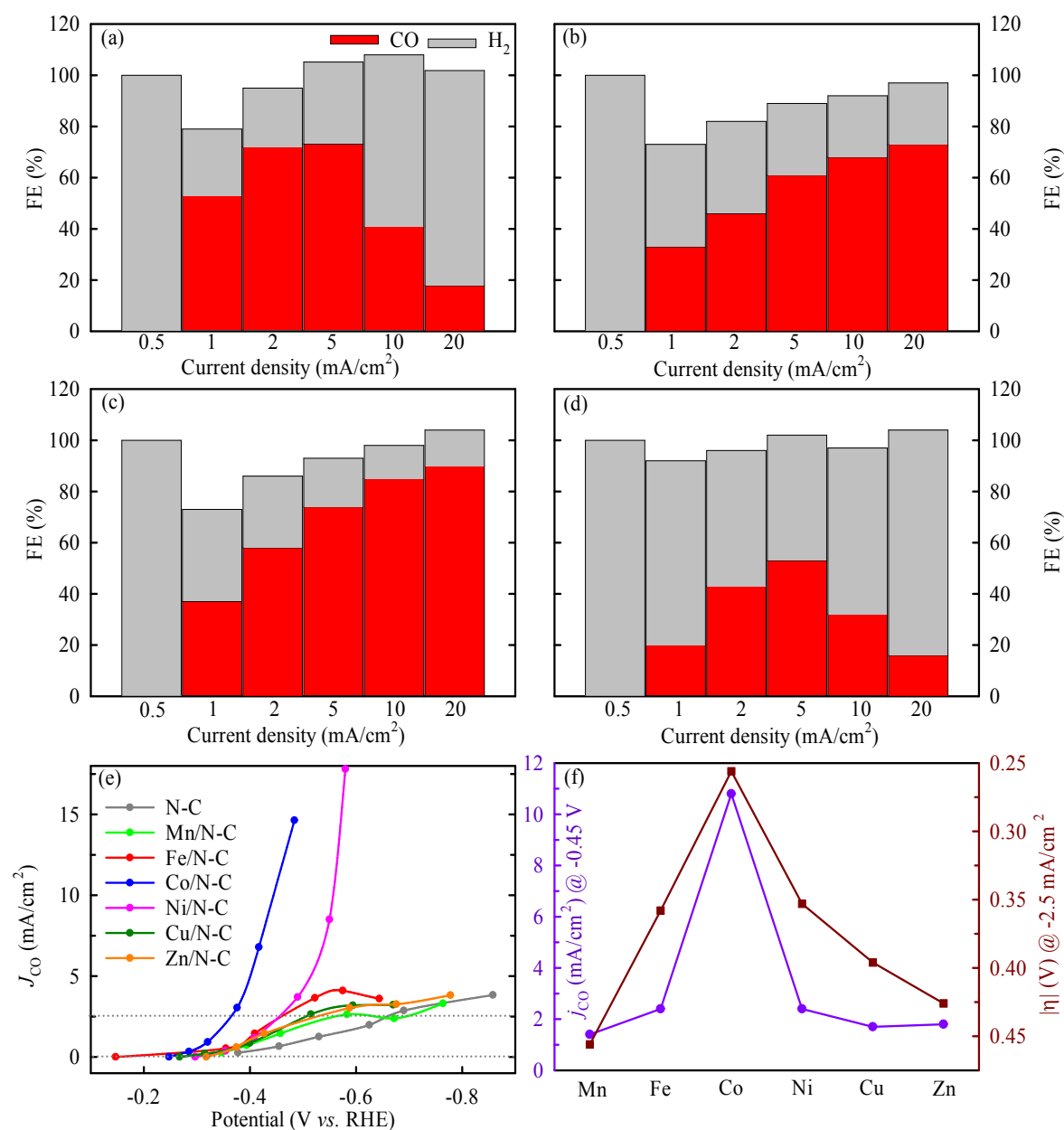
Figure 5. The Faradaic efficiencies for CO and H$_2$ measured in a flow cell as a function of the current density for the down-selected Fe/N-C (a), Co/N-C (b), Ni/N-C (c) and Cu/N-C (d), and the derived polarization curves of CO partial current density *vs.* cathode potential for all materials (e). (f) The volcano trends in eCO$_2$RR activity for M/N-C catalysts: CO partial current density at −0.45 V *vs.* RHE (left handside y-axis) and cathode overpotential at –2.5 mA·cm^{-2} (right handside y-axis). The CO partial current density and overpotential shown in **Figure 5f** is extracted from **Figure 5e** by interpolation. The data were obtained under galvanostatic control for ~90 min in 1 M KHCO$_3$ at room temperature. CO$_2$ gas was supplied

at the back of the gas diffusion electrode whose microporous side was coated with 1 mg·cm^{-2} of catalyst, while the anode was IrO_x. The potential and overpotential reported in e and f are iR-corrected.

To identify trends, we then plotted the J_{CO} at –0.45 V vs. RHE and the cathode overpotential (η) at –2.5 mA·cm^{-2} (CO partial current density) *vs*. the atomic number of transition metal (**Figure 5f**). Interestingly, with increasing atomic number from Mn to Co, J_{CO} monotonically increases, whereas with further increasing atomic number of the metal, the J_{CO} decreases. A similar trend is also apparent for the overpotential at –2.5 mA·cm^{-2}. Similar volcano trends are obtained if one uses the redox potential M^{2+}/M as x-axis. Herein, we reveal a volcano trend in the electrocatalytic activity for the CO_2 to CO reduction over a series of catalysts characterised, *ex situ*, with M/N-C materials comprising highly dispersed MO_x sites in *ex situ* conditions, with Co/N-C located at the volcano peak. This volcano trend is similar to that observed over M-N-C catalysts with M-N$_4$ sites.[25]

While the high activity and selectivity for eCO$_2$RR to CO of the three most active catalysts, Fe-, Co- and Ni/N-C, can be related to the (sub)-nano MO_x structures identified *ex situ*, whether the nitrogen plays a role during the synthesis or during eCO$_2$RR of those M/N-C catalysts is still elusive. Therefore, we prepared nitrogen-free FeO_x/C material by precipitating FeO_x on Vulcan XC72 carbon black powder (labelled as FeO_x/Vulcan), following the same protocol as before. This reference material was characterised *ex situ* by XAS and its eCO$_2$RR activity was measured in the flow cell. The FeO_x/Vulcan shows FT-EXAFS and XANES spectra similar to those of Fe/N-C catalysts (**Figure S7a-b**). This demonstrates the presence of the metal as (sub)nano-oxide, as intended. The Fe content measured from the edge jump of its XAS spectrum (**Table S1**) confirm that FeO_x/Vulcan has a metal content comparable to Fe/N-C. Negligible eCO$_2$RR to CO activity is observed for FeO_x/Vulcan when tested in flow cell under

the same conditions as M/N-C, with H_2 as the major product (**Figure S7c**). It has been reported that Fe^{3+} species from iron oxyhydroxides supported on carbon were *operando* reduced into metallic particles,[26] while the same Fe^{3+} species supported on N-C were only reduced to 2+ oxidation state. Fe^0 is probably responsible for the high selectivity toward H_2 production of FeO_x/Vulcan, since Fe^0 is not known to catalyse CO_2 reduction selectively, even as nanoparticles (it should be noted here that this might not be the case for other metals). These results show that supporting the metal oxide particles on N-C is key to their CO_2RR activity and selectivity, due to similar Fe K-edge XAS spectra and Fe content identified *ex situ* for Fe/N-C and FeO_x/Vulcan, but different activity and selectivity (**Figure 5** and **S7**).

Therefore, a synergy between N-defects or ZnN_x and the MO_x (sub)nano clusters seems to be at play. R. Arrigo *et al.*[26] found from theoretical simulations that pyridinic N defects in N-C lowers the interface energy between iron oxyhydroxide and carbon support, indicating the possible direct interaction between the N-defects and the MO_x species. A synergy between N defects and FeO_x sites was proposed to promote C-C coupling for acetic acid production.[26] Moreover, P. Atanassov *et al* confirmed with near ambient pressure XPS that pyridinic and hydrogenated (pyrrolic) nitrogen moieties, rather than $Fe-N_4$ moieties, act as preferential adsorption sites for CO_2 over pyrolyzed Fe-N-C catalysts[73]. Thus, it is likely that the MO_x species and the neighbouring N-defects co-catalyse the eCO_2RR. Moreover, further work will be needed to elucidate whether Zn plays a role (direct or indirect) in stabilizing such hydroxides particles or not.

2.3 Structural changes of MO_x sites identified with *operando* XAS

To gain more insights in the fate of the metal-oxide nanoparticles supported on N-C, we resorted to *in operando* XAS. It is widely acknowledged that metal-based electrocatalysts often experience partial reduction and/or structural reconstruction during eCO_2RR.[17, 26, 42, 74, 75] This

can be due to the low electrochemical potential, *operando* produced H_2 gas and/or *operando* produced CO. The latter is known to facilitate reconstruction of metal surfaces, and agglomeration of NPs.[43] For M-N-C materials prepared by pyrolysis and comprising only MN_4 moieties *ex situ*, we recently reported a decreased average oxidation state of Fe and Ni within MN_4 moieties and reduction of a large fraction of $Cu^{2+}N_x$ sites to Cu(0), *via* the reversible formation of Cu (sub)nanoparticles, with decreasing electrochemical potential under eCO_2RR working conditions.[25, 55] To identify the local structures of transition metals sites under operating conditions, we therefore conducted *operando* XAS on the series of M/N-C catalysts.

We first studied the N-C substrate (comprising ZnN_x moieties, **Figure S1**) at the Zn K-edge. The Zn K-edge XANES spectra show only a slight decrease in white line intensity with decreasing potential (**Figure S8a-b**). A similar behaviour is observed for Zn/N-C (**Figure S8c-d**). By extrapolation, this suggests a slightly reduced average oxidation state of Zn in M/N-C and M-N-C catalysts with decreasing potential. This can be assigned to the *operando* formation of a very small amount of metallic Zn nanoparticles. Regarding Mn/N-C, the structure remains unchanged till -1.0 V *vs*. RHE (**Figure S8e-f**). Overall, the *operando* observations with Zn and Mn are in line with their Pourbaix diagrams, with no or minimal reduction of the metal expected before -0.76 V and -1.2 V *vs*. RHE, respectively.

In contrast, the *operando* XAS spectra of Fe/, Co/, Ni/ and Cu/N-C are different from those measured *ex situ* (**Figure 6** and **S9-10**), in line with their much higher M^{2+}/M redox potential. To start with the simplest case, the Cu K-edge XANES spectrum of Cu/N-C shifts toward lower energies with decreasing potential, corresponding to a decreased average oxidation state (**Figure 6a**). This is accompanied by the appearance of a signal that can be assigned to the Cu-Cu coordination, by comparison with the FT-EXAFS of a Cu foil (**Figure 6b**). This

demonstrates the reduction from Cu^{2+} to nearly Cu^0 with an extensive formation of metallic copper clusters during eCO_2RR, even at 0 V *vs*. RHE, well above the onset of eCO_2RR on Cu/N-C ($\sim$ –0.4 V *vs*. RHE). The formation of Cu nanoparticles is reversible, as shown by the spectrum of OCP-back overlapping with that of OCP (**Figure S9a-b**). A minor Cu-N/O peak around 1.5 Å is visible at low potentials, indicating that a small fraction of copper atoms binds with N or O surface groups from N-C (**Figure 6b**). The anchoring of some Cu atoms to both the N-C support and the *operando* formed Cu^0 nanoparticles could explain the restricted particle growth and the observed reversibility with Cu re-dispersion at high potential. The *operando* formation of Cu^0 nanoparticles has been widely observed on other Cu-based catalysts comprising isolated Cu atoms *ex situ*;[56, 76, 77] and these Cu^0 nanoparticles very likely act as the catalytically active species. Recently, T. Möller *et al* revealed that Cu nanoparticles supported on carbon favour the formation of C_1 product instead of the C_{2+} products generally observed on unsupported Cu[78]. The selectivity towards C_1 product with Cu nanoparticles is due to the large mean interparticle distance for particles supported in low wt% on a high surface area support material, in line with our finding that CO is the major product in this potential range over the *operando* formed Cu^0 supported on N-C.

For Ni/N-C, the XANES and FT-EXAFS spectra remain unchanged when the potential was reduced from OCP to 0 V *vs*. RHE, and these spectra are close to those measured *ex situ*, assigned to NiO clusters. From 0 to –0.5 V *vs*. RHE, the XANES spectra then show a gradual decrease in white line intensity and increase in the pre-edge peak intensity at $\sim$8334 eV (**Figure 6c** and **S10a**). The intensity of the pre-edge peak at 8334 eV stays the same at all potentials $\leq$ –0.5 V *vs*. RHE, and is indicative of the formation of highly distorted octahedral or tetrahedral Ni-O_x coordination in nickel hydroxides (**Figure 6c** and **S10a**).[79, 80] In contrast, in FT-EXAFS a new intense peak progressively appears at $\sim$2.5 Å from –0.4 V to –1.0 V *vs*. RHE (**Figure S9d**), and that can be assigned to Ni-Ni_{oxy} interaction in Ni hydroxide. In addition, the

22

appearance of a shoulder at ~2 Å at–1.0 V *vs.* RHE (**Figure 6c**), a position corresponding to

Ni-Ni interaction in the metallic Ni foil, suggests the minor formation of metallic Ni at the

lowest potential. Overall, the data suggests the transformation from (sub)nano-NiO *ex situ* to

(sub)nano-Ni(OH)$_2$ at –0.4 V *vs.* RHE, and then clustering to larger Ni(OH)$_2$ nanoparticles at

even lower potential. Moreover, there is a phase contraction of the material at low potential

compared to Ni(OH)$_2$, as evidenced by the shorter Ni-O and Ni-Ni$_{oxy}$ bond distances compared

to those of Ni(OH)$_2$ reference (*e.g.* at –0.5 and –1.0 V *vs.* RHE, **Figure 6d** and **Figure 7**). We

note that this phase contraction has been widely observed for nickel-based catalysts during

oxygen evolution reaction (OER),[81, 82] attributed to the oxidized nature of Ni at high potentials.

We for the first time, to the best of our knowledge, report similar phase contraction of nickel

hydroxides, but at reducing potentials. The lattice contraction may be due to cation vacancies

introduced by partially reduced nickel, and/or due to the intercalation of water and bicarbonate

ions into the layered structures of nickel hydroxides.[83-85] Upon reverting the potential from –

1 V *vs.* RHE to OCP (OCP-back curves), the XANES and FT-EXAFS spectra were largely

restored to the initial OCP spectrum (**Figure S9c-d**), suggesting the reversibility of this process.

The absorption edge in the XANES spectrum of Co/N-C remains largely unchanged with

potential from OCP to 0 and –0.3 V *vs.* RHE, while the white line intensity slightly increases

(**Figure 6e** and **Figure S9e**). The latter can be explained by a transition from cobalt oxide to

cobalt hydroxide phase, as can be seen by comparison to the white line intensities for the

reference spectra for the latter (compare **Figure S3b** and **6e**). The XANES spectra at –0.5 and

–1.0 V *vs.* RHE show a decreased white line intensity and an increased pre-edge feature

(~7710–7714 eV) intensity, indicative of the partial reduction of Co into Co^0 species (**Figure

6e** and **S10b**). The broad Co-O peak in the corresponding FT-EXAFS spectra seen at high

potential at ~1.5 Å (with a shoulder ~1.7 Å) splits into two distinct peaks at 1.2 and 1.7 Å at –

0.5 V *vs.* RHE and below (**Figure 6f**). These two peaks are possibly assigned to Co-O

interaction from octahedral Co^{2+} and Co-O or Co-C interaction from tetrahedral Co^{2+}, respectively. It should be noted here that splitting of a FT-EXAFS peak can also be explained by the destructive interferences due to the (dis)appearance of phases. Tetrahedral CoX_4 structure has been reported for layered $Co(OH)_2$, where in the Co^{2+} coordinates with O and/or C from intercalated water and HCO_3^- cations between CoO_6 layers.[86] The intercalated water and cations also induce the phase contraction of $Co(OH)_2$, as evidenced by the shorter Co-O and $Co-Co_{oxy}$ peak in Co/N-C than in reference $Co(OH)_2$ (**Figure 6f**). The critical role of HCO_3^- cations, instead of gas-phase CO_2, during eCO_2RR has been observed over Au and Cu.[87, 88] Interestingly, the intensity of the peak arising from $Co-Co_{oxy}$ in the FT-EXAFS spectra first increases at −0.5 V *vs*. RHE induced by the clustering of Co sites; and then decreases at −1.0 V *vs*. RHE, probably due to the potential-induced reversible amorphization of cobalt oxide reported previously.[89] The XANES spectrum reverts to the spectrum of 0 V *vs*. RHE at the end of the series of applied potentials, while the Co-O peak in the FT-EXAFS spectrum remains split, different from the initial OCV FT-EXAFS (**Figure S9e-f**). This suggests that the intercalated structure was maintained for at least some time after removing the potential bias.

Regarding Fe/N-C (**Figure 6g**), there is a negative shift in the position of the absorption edge of Fe K-edge XANES spectra of ~2 eV from OCP to 0 V *vs*. RHE, indicative of a Fe^{3+} to Fe^{2+} reduction; and then the XANES spectra remain the same till −0.4 V *vs*. RHE (**Figure S9g**). When the potential is further lowered to −1.0 V *vs*. RHE, the white line intensity gradually decreases, accompanied with an increased pre-edge peak (~7115 eV) intensity (**Figure S10c**). This enhanced pre-edge peak is indicative of the partial reduction of Fe^{2+} to Fe^0 species. As for Co/N-C, the Fe-N/O peak in the corresponding FT-EXAFS spectra also splits into two peaks at 1.1 and 1.8 Å (**Figure 6h**). This effect was observed previously by R. Arrigo *et al*. as well.[26] The FT-EXAFS $Fe-Fe_{oxy}$ peak first decreases in intensity till −0.4 V *vs*. RHE due to a decreased

particle size of iron hydroxide (**Figure S9h**); and then shifts toward lower R value below –0.5

V *vs*. RHE, due to phase contraction (**Figure 6h and S9h**). The changes in oxidation states

observed in the XANES spectra of Fe/N-C are largely reversible when the potential is reverted

back to OCP (**Figure S9g**), while the split Fe-O peak due to the phase contraction remain to

some extend (**Figure S9h**).
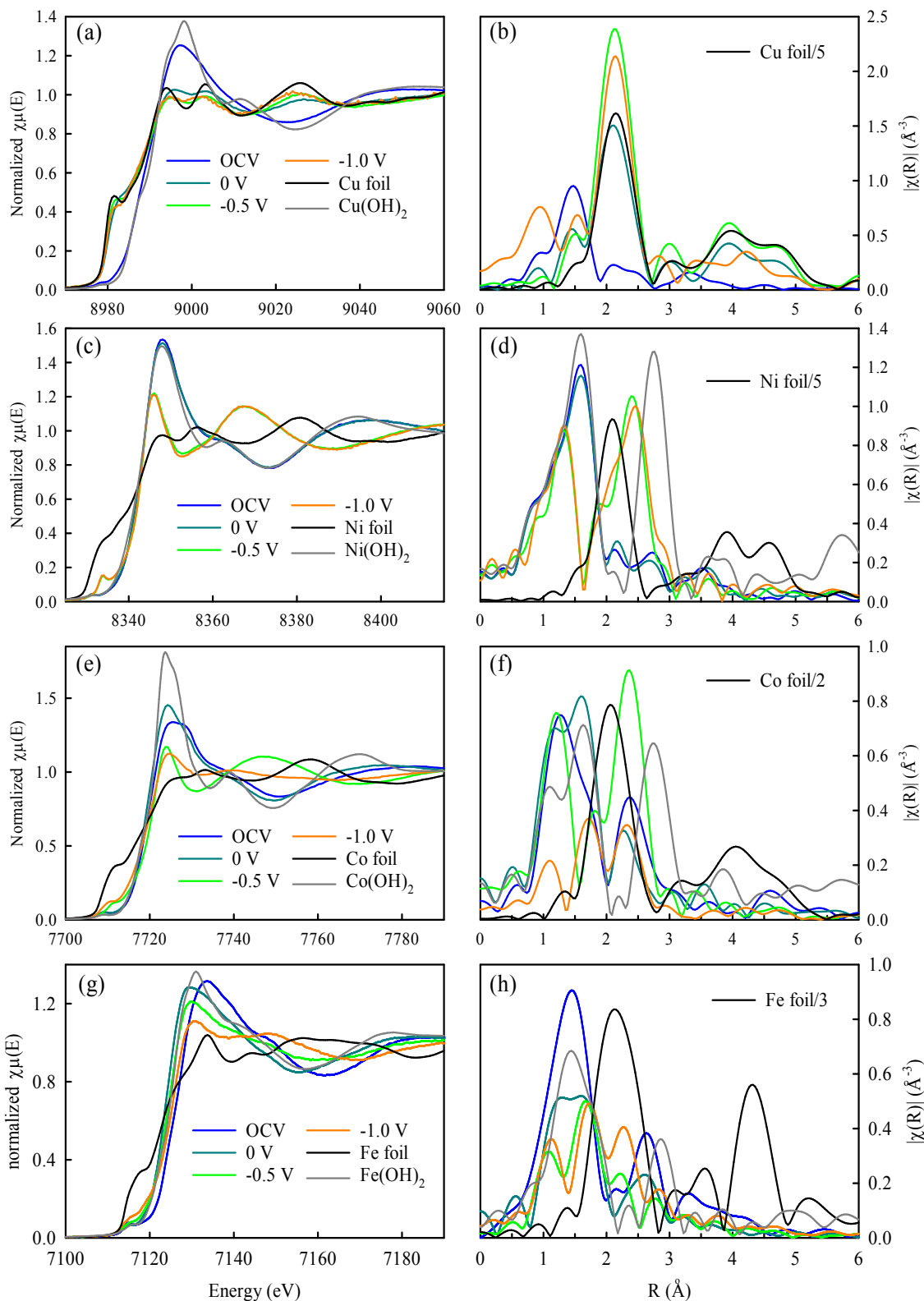
Figure 6. The *operando* XANES and FT-EXAFS spectra for M/N-C materials (M = Fe, Co, Ni, Cu) and their comparison to reference spectra of metal-hydroxides and metallic foils. *Operando* XANES spectra for Cu/N-C (a), Ni/N-C (c), Co/N-C (e) and Fe/N-C (g). *Operando*

FT-EXAFS spectra for Cu/N-C (b), Ni/N-C (d), Co/N-C (f) and Fe/N-C (h) and comparison to the spectra for metal-hydroxides or metallic foils.

In summary, the majority of Cu atoms in Cu/N-C forms Cu^0 clusters during eCO_2RR; while the Mn/, Fe/, Co/, and Ni/N-C maintain the metal hydroxide structures, with a minor amount of M^0 formed in Fe-, Co-, and Ni-based samples. The unexpected information from *operando* XAS is that the vast majority of Ni, Co and Fe nano-oxides were not reduced to metallic particles, even at -1 V *vs.* RHE, which is 550 to 750 mV lower than the values expected according to the Pourbaix diagrams. In contrast, most metal atoms in Ni-, Fe- and Co/NC catalysts stay as oxides, but with a phase contraction (**Figure 7**). The M-O peaks in the FT-EXAFS of Fe/ and Co/N-C split into two peaks due to tetrahedral M^{2+} coordination in the intercalated layer, indicating that the HCO_3^- is inserted into the layered structure of metal hydroxides (**Figure 7**). Recently, two independent groups demonstrated the critical role of HCO_3^- ions, through equilibrium exchange with dissolved CO_2, rather than the supplied CO_2, as the primary source for eCO_2RR.[87, 88] Thus, the inserted HCO_3^- cations and/or the phase contraction of metal oxides at working potentials may be responsible for the superior activity of Fe-, Co- and Ni/N-C catalysts.
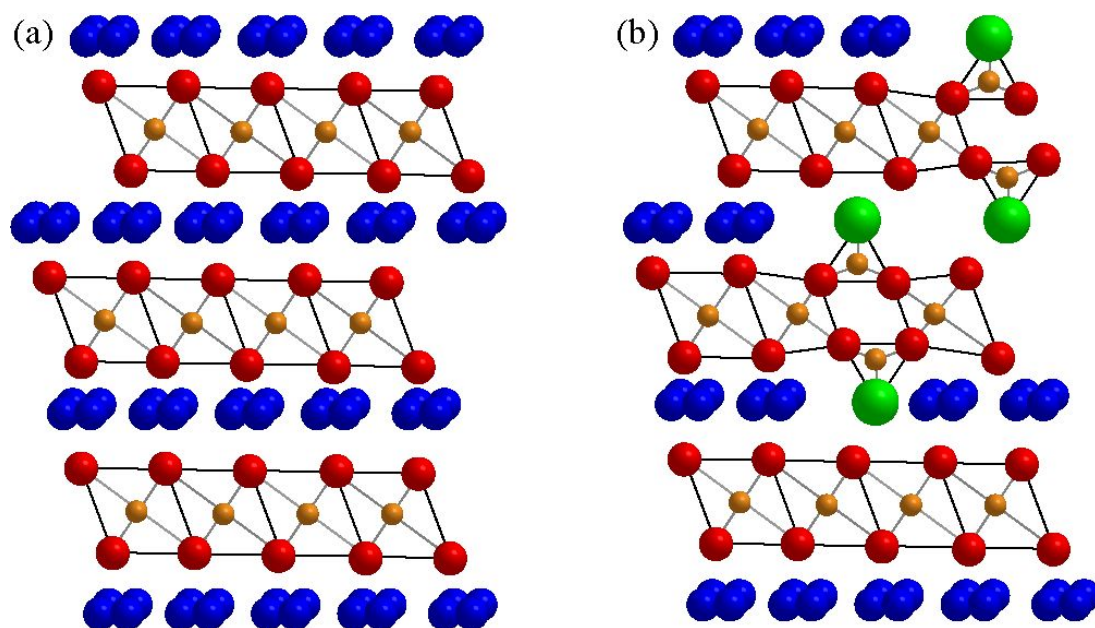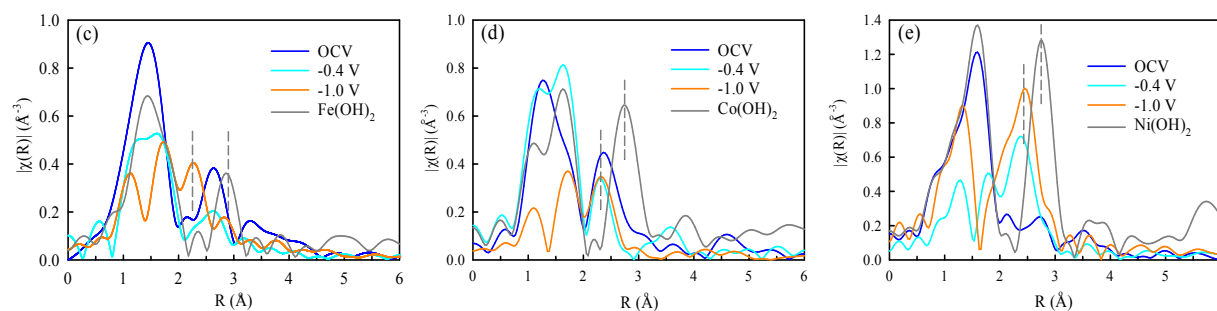
Figure 7. The scheme illustrating the phase contraction and structural distortion of $M(OH)_2$ induced by the intercalation of HCO_3^- (modified from Ref. 86). The structures of $M(OH)_2$ without (a) and with (b) cathodic potential bias. Species for M, OH, HCO_3^-, and H_2O are represented by orange, red, green, and blue spheres, respectively. The insertion of HCO_3^- leads to the distortion of MO_6 octahedra and the appearance of tetrahedral MO_4 with different M-O bond distances, as evidenced by the splitting of M-O peaks. The insertion of HCO_3^- is also accompanied with shortened M-O and $M-M_{oxy}$ bond distances. The splitting of M-O peaks with decreasing potential of Fe/N-C (c) and Co/N-C (d), as well as the shortened M-O and/or $M-M_{oxy}$ bond distances in Fe/N-C (c), Co/N-C (d) and Ni/N-C (e) *vs.* $M(OH)_2$ references are shown from selected *operando* FT-EXAFS.

2.3 Optimized flow cell with M/N-C cathodes and NiFe-based anodes

The intrinsic activity and selectivity of Ni/N-C toward CO_2RR to CO are comparable to those of the state-of-the-art Au, Ag, and M-N-C catalysts (**Table S4**). M/N-C and M-N-C materials hold great potential to lower the cost of CO_2 electrolyzer by replacing the expensive precious metal-based catalysts (e.g., Au and Ag). Moreover, the advantage of M/N-C over M-N-C lies not only in the facile and controlled synthesis of the former, but also the possible reactivation of M/N-C materials after degradation (reduction), since the reconversion of metallic nanoparticles into metal hydroxide form should be easier than the reconversion of a metallic cluster back into MN_x sites. However, even with the most promising M/N-C (Fe, Co, or Ni) cathode and flat IrO_x anode, the total cell voltage is above 3 V at 20 mA/cm^2 (**Figure S11**),

with a large overpotential likely arising also at the anode side. To decrease the overpotential for the oxygen evolution reaction (OER) and remove precious metals from the cell, we implemented a high surface area Ni-Fe oxyhydroxide anode prepared on a Ni foam (NF) *via* a phosphidation process, labelled as NF/Ni$_2$P/Ni-FeO$_x$ (see synthesis in Experimental Methods)[90].

The porous backbone of NF is observed in the micro-computed tomography (CT) (**Figure S12a**) and scanning electron microscopy (SEM) (**Figure S13a**) images, and the NiFe-based OER catalyst was decorated homogeneously on the Ni foam (**Figure S12a**). The XRD pattern exhibits two strong peaks assigned to NF, two minor peaks arising from Ni$_2$P, and no peak of the Ni-Fe phase (**Figure S13b**); while the presence of Fe, P and O is clearly evidenced in energy dispersive X-ray spectroscopy (EDX) and electron energy loss spectroscopy (EELS) mapping (**Figure S13c** and **S14a**). This indicates the amorphous nature of the Ni-Fe oxyhydroxide in the catalyst, further supported by high resolution (HR)-TEM images, showing a crystalline phase of hexagonal Ni$_2$P in the core and another amorphous phase on the edges (**Figure S14b-c**). The OER activity of NF/Ni$_2$P/Ni-FeO$_x$ was first evaluated with rotating disk electrode (RDE) in KOH (0.1 and 1 M) and KHCO$_3$ (1 M) in comparison with IrO$_2$ supported on Ni foam. **Figure S15a-c** demonstrates that the OER activity of NF/Ni$_2$P/Ni-FeO$_x$ is superior to that of IrO$_2$ in all electrolytes, and that the overpotential for the former at 10 mA·cm^{-2} reduces with increasing pH, reaching ~240 mV in 1 M KOH (**Figure S15b**). Moreover, the overpotential at 10 mA·cm^{-2} was further reduced by ~100 mV after an accelerated stability test (AST) (**Figure S15d**). No obvious changes in the morphology and structure of NF/Ni$_2$P/Ni-FeO$_x$ were observed by X-CT, SEM, XRD, and HRTEM (**Figure S12-13** and **S16**). Its impressive activity and stability make it appealing to implement in electrolyzers, and a significant decrease in total cell voltage up to ~1 V was observed after replacing IrO$_2$ anode

with NF/Ni$_2$P/Ni-FeO$_x$ in a CO$_2$ electrolyzer with Ni-N-C as cathode and 1 M KHCO$_3$ as electrolyte (**Figure S11**).

We investigated the activity and selectivity of Fe/, Co/ and Ni/N-C cathodes with NF/Ni$_2$P/Ni-FeO$_x$ anode (**Figure 8**). Since the anode catalyst is more active at higher pH, we used 1 M KOH instead of KHCO$_3$ as anolyte and catholyte in the following study. Co- and Ni/N-C exhibit similar cell voltages for a given current density, lower than that of Fe/N-C. However, Ni/N-C exhibits a higher FE than Co/N-C, reaching a FE(CO) >90% at 50 mA·cm^{-2}. A FE(CO) >80% is even maintained over Ni/N-C at 100 mA·cm^{-2} total current density, with a total cell voltage of ~4 V. It should be noted here that a large portion of the cell voltage comes from the iR-drop due to the thick layers of electrolyte in the commercial cell. The total cell resistance is > 25 Ω·cm^2 as measured by high frequency resistance, while that estimated for the liquid chambers is ~10 Ω·cm^2 (from *circa* 2 cm thickness of anolyte + catholyte, electrolyte conductivity of ~200 mS·cm^{-1} for 1 M KOH). Thus, the total cell voltage could be further reduced through cell design, *e.g.* reducing the thickness of each electrolyte chamber possibly down to zero-gap configuration, or increasing the temperature.

When the total current density was increased from 100 to 150 mA·cm^{-2}, a sharp decrease in FE was observed. Similar behaviour has been observed over Ni-N-C as well. This is probably due to CO$_2$ depletion at the catalytic sites, leading to competitive HER. This can be improved by increasing the CO$_2$ backpressure. P. Strasser *et al.*[16] reported a stable current density as high as 200 mA·cm^{-2} over Ni-N-C catalysts with the same flow cell, by closing the CO$_2$ gas out to force the CO$_2$ passing through the GDE, resulting in pressurized CO$_2$ gas flow. Moreover, we also noticed some particles in the anolyte, indicating the mechanical instability of the anode during strong O$_2$ evolution. This suggests that improved mechanical robustness of the anode during strong gas evolution is also important for cell stability.
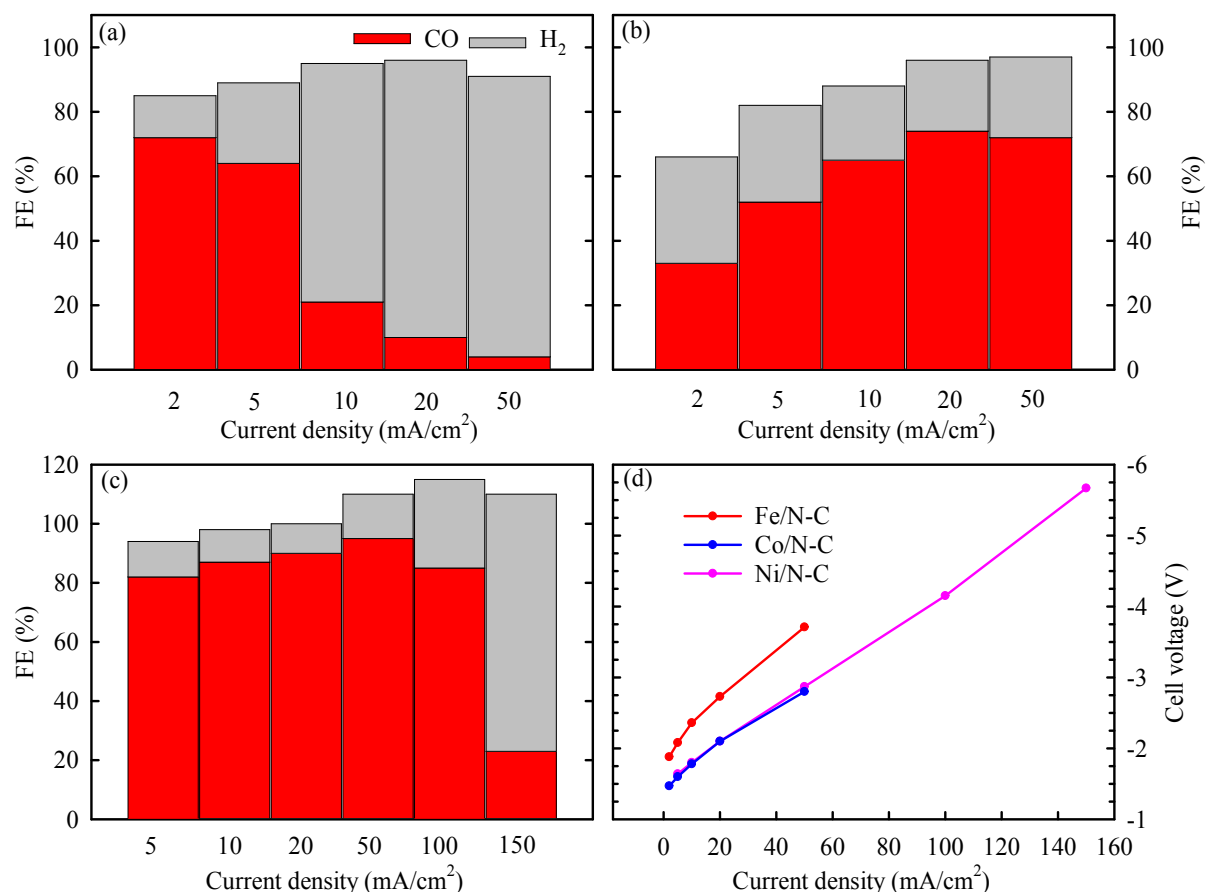
Figure 8. The Faradaic efficiencies of flow cell measurements with $NF/Ni_2P/Ni\text{-}FeO_x$ anode

and M/N-C cathodes (Fe (a), Co (b) and Ni (c)), and (d) the polarization curve of cell voltage

vs. total current density. Data were acquired in flow cell with 1 M KOH aqueous catholyte and

anolyte at room temperature, and the CO_2 gas was fed at the back of GDE.

In summary, we have synthesized a series of M/N-C catalysts with highly dispersed MO_x

particles supported on nitrogen-doped carbon, and evaluated their activity and selectivity

toward eCO_2RR to CO in a flow cell with GDE. We reveal a volcano-shaped trend in the

electrocatalytic activity for CO over M/N-C catalysts, which is similar to that reported for M-

N-C catalysts with atomically-dispersed $M\text{-}N_4$ sites. *Operando* XAS shows that the metal

(hydr)oxide clusters in M/N-C largely remain as contracted hydroxides at –1 V *vs.* RHE in

Fe/N-C, Co/N-C and Ni/N-C, with the parallel formation of a minor amount of metallic species.

These metal hydroxides experience phase contractions and the insertion of H_2O/HCO_3^- into

31

their layered structures. Last, flow cell measurements with M/N-C cathodes and state-of-the-art NiFe-anodes were performed, and Ni/N-C exhibits >80% FE toward CO at 100 mA/cm^2 with a total cell voltage of ~4 V.

32

ASSOCIATED CONTENT

AUTHOR INFORMATION

Corresponding Author

* To whom correspondence should be addressed. Email: frederic.jaouen@umontpellier.fr

Author Contributions

J.L. and F.J. designed, synthesized and physically characterized the materials. F.A.G.-P., P.T, J.A., and J.R.G.-M. processed and characterized the NiFe-based OER catalysts and electrodes. P.T. and J.A. conducted the HRTEM and STEM-EELS characterization of NiFe-based anodes. J.L. and F.J. also performed the eCO_2RR electrochemical measurements and product analysis. T.A., and P.A. conducted the STEM characterizations of M/N-C materials. I.Z. performed the X-CT experiments and analysis. J.L. and A.Z. conducted the *ex situ* and *operando* XAS experiments. T.A., M.K. and P.A. conducted the XPS measurement and analysis. M.T.S. performed the Mössbauer spectroscopy measurements and analysis. J.L., A.Z. and F.J. wrote and edited the manuscript with input from all authors. All authors read and approved the final version of the manuscript.

Programme / Generalitat de Catalunya. ICN2 and ICIQ are supported by the Severo Ochoa

program from Spanish MINECO (Grants No. SEV-2017-0706 and CEX2019-000925-S).

Notes

The authors declare no competing financial interest.

Supporting Information.

The following files are available free of charge.

Physical (XRD, STEM, XPS), *ex situ* and *operando* XAS, and electrochemical (FEs and

polarization curves obtained from flow cell tests) characterizations of M/N-C catalysts for

eCO_2RR or NiFe-based catalysts for OER (PDF)

34

REFERENCES

1. Fan, L.; Xia, C.; Yang, F.; Wang, J.; Wang, H.; Lu, Y. Strategies in Catalysts and Electrolyzer Design for Electrochemical CO_2 Reduction toward C_{2+} Products. *Sc. Adv.* **2020**, *6*, eaay3111.

2. Ma, M.; Clark, E.L.; Therkildsen, K.T.; Dalsgaard, S.; Chorkendorff, I.; Seger, B. Insights into the Carbon Balance for CO_2 Electroreduction on Cu using Gas Diffusion Electrode Reactor Designs. *Energy & Environ. Sci.* **2020**, *13*, 977-985.

3. Burdyny, T.; Smith, W.A. CO_2 Reduction on Gas-Diffusion Electrodes and Why Catalytic Performance Must Be Assessed at Commercially-Relevant Conditions. *Energy & Environ. Sci.* **2019**, *12*,1442-1453.

4. Nam, D.-H.; Nam, D.-H.; Luna, P.D.; Rosas-Hernández, A.; Thevenon, A.; Li, F.; Agapie, T.; Peters, J.C.; Shekhah, O.; Eddaoudi, M.; Sargent, E.H. Molecular Enhancement of Heterogeneous CO_2 Reduction. *Nat. Mater.* **2020**, *19*, 266-276.

5. Wei, X.; Yin, Z.; Lyu, K.; Li, Z.; Gong, J.; Wang, G.; Xiao, L.; Lu, J.; Zhuang, L. Highly Selective Reduction of CO_2 to C_{2+} Hydrocarbons at Cu/Polyaniline Interfaces. *ACS Catal.* **2020**, *10*, 4103-4111.

6. Clark, E.L.; Hahn, C.; Jaramillo, T.F.; Bell, A.T. Electrochemical CO_2 Reduction over Compressively Strained CuAg Surface Alloys with EEnhanced Multi-Carbon Oxygenate Selectivity. *J. Am. Chem. Soc.* **2017**, *139*, 15848-15857.

7. Calle-Vallejo; F.; Koper, M.T.M.; Bandarenka, A.S. Tailoring the Catalytic Activity of Electrodes with Monolayer Amounts of Foreign Metals. *Chem. Soc. Rev.* **2013**, *42*, 5210-5230.

8. Zhou, Y.; Che, F.; Liu, M.; Zou, C.; Liang, Z.; Luna, P.D.; Yuan, H.; Li, J.; Wang, Z.; Xie, H.; Li, H.; Chen, P.; Bladt, E.; Quintero-Bermudez, R.; Sham, T.-K.; Bals, S.; Hofkens, J.; Sinton, D.; Chen, G.; Sargent, E.H. Dopant-Induced Electron Localization Drives CO_2 Reduction to C_2 Hydrocarbons. *Nat. Chem.* **2018**, *10*, 974-980.

9. Luo, W.; Nie, X.; Janik, M.J.; Asthagiri, A. Facet Dependence of CO_2 Reduction Paths on Cu Electrodes. *ACS Catal.* **2016**, *6*, 219-229.

10. Tang, W.; Peterson. A.A.; Varela, A.S.; Jovanov, Z.P.; Bech, L.; Durand, W.J.; Dahl, S.; Nørskov, J.K.; Chorkendorff, I. The Importance of Surface Morphology in Controlling the Selectivity of Polycrystalline Copper for CO_2 Electroreduction. *Phys. Chem. Chem. Phys.* **2012**, *14*, 76-81.

11. Loiudice, A., Lobaccaro, P.; Kamali, E.A.; Thao, T.; Huang, B.H.; Ager, J.W.; Buonsanti, R. Tailoring Copper Nanocrystals towards C_2 Products in Electrochemical CO_2 Reduction. *Angew. Chem. Int. Ed.* **2016**, *55*, 5789-5792.

12. Yin, Z.; Peng, H.; Wei, X.; Zhou, H.; Gong, J.; Huai, M.; Xiao, L.; Wang, G.; Lu, J.; Zhuang, L. An Alkaline Polymer Electrolyte CO_2 Electrolyzer Operated with Pure Water. *Energy & Environ. Sci.* **2019**, *12*, 2455-2462.

13. Dinh, C.-T.; Burdyny, T.; Kibria, M.G.; Seifitokaldani, A.; Gabardo, C.M.; Arquer, F.P.G.; Kiani, A.; Edwards, J.P.; Luna, P.D.; Bushuyev, O.; Zou, C.; Quintero-Bermudez, R.; Pang, Y.; Sinton, D.; Sargent, E.H. CO_2 Electroreduction to Ethylene via Hydroxide-Mediated Copper Catalysis at an Abrupt Interface. *Science* **2018**, *360*, 783-787.

14. Xia, C.; Zhu, P.; Jiang, Q.; Pan, Y.; Liang, W.; Stavitski, E.; Alshareef, H.N.; Wang, H. Continuous Production of Pure Liquid Fuel Solutions via Electrocatalytic CO_2 Reduction using Solid-Electrolyte Devices. *Nat. Energy*, **2019**, *4*, 776-785.

15. Chen, C.; Kotyk, J.F.K.; Sheehan, S.W. Progress toward Commercial Application of Electrochemical Carbon Dioxide Reduction. *Chem* **2018**, *4*, 2571-2586.

16. Möller, T.; Ju, W.; Bagger, A.; Wang, X.; Luo, F.; Thanh, T.N.; Varela, A.S.; Rossmeisl, J.; Strasser, P. Efficient CO_2 to CO Electrolysis on Solid Ni–N–C Catalysts at Industrial Current Densities. *Energy & Environ. Sci.* **2019**, *12*, 640-647.

17. Jeon, H.S.; Sinev, I.; Scholten, F.; Divins, N.J.; Zegkinoglou, I.; Pielsticker, L.; Cuenya, B.R. *Operando* Evolution of the Structure and Oxidation State of Size-Controlled Zn Nanoparticles during CO$_2$ Electroreduction. *J. Am. Chem. Soc.* **2018**, *140*, 9383-9386.

18. Dutta, A.; Morstein, C.E.; Rahaman, M.; López, A.C.; Broekmann, P. Beyond Copper in CO$_2$ Electrolysis: Effective Hydrocarbon Production on Silver-Nanofoam Catalysts. *ACS Catal.* **2018**, *8*, 8357-8368.

19. Cao, Z.; Zacate, S.B.; Sun, X.; Liu, J.; Hale, EE.M.; Carson, W.P.; Tyndall, S.B.; Xu, J.; Liu, X.; Liu, X.; Song, C.; Luo, J.-H.; Cheng, M.J.; Liu, W. Tuning Gold Nanoparticles with Chelating Ligands for Highly Efficient Electrocatalytic CO$_2$ Reduction. *Angew. Chem. Int. Ed.* **2018**, *57*, 12675-12679.

20. Yuan, T.; Hu, Z.; Zhao, Y.; Fang, J.; Lv, J.; Zhang, Q.; Zhuang, Z.; Gu, L.; Hu, S. Two-Dimensional Amorphous SnO$_x$ from Liquid Metal: Mass Production, Phase Transfer and Electrocatalytic CO$_2$ Reduction towards Formic Acid. *Nano Lett.* **2020**, *4*, 2916-2922.

21. Ju, W.; Bagger, A.; Hao, G.-P.; Varela, A.S.; Sinev, I.; Bon, V.; Cuenya, B.R.; Kaskel, S.; Rossmeisl, J.; Strasser, P. Understanding Activity and Selectivity of Metal-Nitrogen-Doped Carbon Catalysts for Electrochemical Reduction of CO$_2$. *Nat. Commun.* **2017**, *8*, 944.

22. Li, X.; Bi, W.; Chen, M.; Sun, Y.; Ju, H.; Yan, W.; Zhu, J.; Wu, X.; Chu, W.; Wu, C.; Xie, Y. Exclusive Ni–N$_4$ Sites Realize Near-Unity CO Selectivity for Electrochemical CO$_2$ Reduction. *J. Am. Chem. Soc.* **2017**, *139*, 14889-14892.

23. Pan, Y.; Lin, R.; Chen, Y.; Liu, S.; Zhu, W.; Cao, X.; Chen, W.; Wu, K.; Cheong, W.-C.; Wang, Y.; Zheng, L.; Luo, J.; Lin, Y.; Liu, Y.; Liu, C.; Li, J.; Lu, Q.; Chen, X.; Wang, D.; Peng, Q.; Chen, C.; Li, Y. Design of Single-Atom Co–N$_5$ Catalytic ite: aA obust eElectrocatalyst for CO$_2$ Reduction with Nearly 100% CO Selectivity and Remarkable Stability. *J. Am. Chem. Soc.* **2018**, *140*, 4218-4221.

24. Wang, X.; Chen, Z.; Zhao, X.; Yao, T.; Chen, W.; You, R.; Zhao, C.; Wu, G.; Wang, J.; Huang, W.; Yang, J.; Hong, X.; Wei, S.; Wu, Y.; Li, Y. Regulation of Coordination Number over Single Co Sites: Triggering the Efficient Electroreduction of CO$_2$. *Angew. Chem. Int. Ed.* **2018**, *57*, 1944-1948.

25. Li, J.; Prslja, P.; Shinagawa, T.; Fernandez, A.J.M.; Krumeich, F.; Artyushkova, K.; Atanassov, P.; Zitolo, A.; Zhou, Y.; García-Muelas, R.; LopÀez, N.; Perez-Ramírez, J.; Jaouen, F., Volcano Trend in Electrocatalytic CO$_2$ Reduction Activity over Atomically Dispersed Metal ites on niNtrogen-Doped Carbon. *ACS Catal.* **2019**, *9*, 10426–10439.

26. Genovese, C.; Schuster M.E.; Gibson E.K.; Gianolio, D.; Posligua, V.; Grau-Crespo, R.; Cibin, G.; Wells, P.P.; Garai, D.; Solokha, V.; Calderon, S.K.; Velasco-Velez, J.J.; Ampelli, C.; Perathoner, S.; Held, G.; Centi, G.; Arrigo, R. *Operando* Spectroscopy Study of the Carbon Dioxide Electro-Reduction by Iron Species on Nitrogen-Doped Carbon. *Nat. Commun.* **2018**, *9*, 935.

27. De, R.; Gonglach, S.; Paul, S.; Haas, M.; Sreejith, S.S.; Gerschel, P.; Apfel, U.-P.; Vuong, T.-H.; Rabeah, J.; Roy, S.; Schöfberger, W. Electrocatalytic Reduction of CO$_2$ to Acetic Acid by a Molecular Manganese Corrole Complex. *Angew. Chem. Int. Ed.* **2020**, *59*, 10527-10534.

28. Lv, K.; Lv, K.; Fan, Y.; Zhu, Y.; Yuan, Y.; Wang, J.; Zhu, Y.; Zhang, Q. Elastic Ag-Anchored N-Doped Graphene/Carbon Foam for the Selective Electrochemical Reduction of Carbon Dioxide to Ethanol. *J. Mater. Chem. A* **2018**, *6*, 5025-5031.

29. Wang, Y.; Wang, Z.; Dinh, C.-T.; Li, J.; Ozden, J.; Kibria, M.G.; Seifitokaldani, A.; Tan, C.-S.; Gabardo, C.-M.; Luo, M.; Zhou, H.; Li, F.; Lum, Y.; McCallum, C.; Xu,Y.; Liu, M.; Proppe, A.; Johnston, A.; Todorovic, P.; Zhuang, T.-T.; Sinton, D.; Kelley, S.O.; Sargent, E.H. Catalyst Synthesis under CO$_2$ Electroreduction Favours Faceting and Promotes Renewable Fuels Electrosynthesis. *Nat. Catal.* **2020**, *3*, 98-106.

30. Liang, Z.-Q.; Zhuang, T.-T.; Seifitokaldani, A.; Li, J.; Huang, C.-W.; Tan, C.-S.; Li, Y.; Luna, P.D.; Dinh, C.-T.; Hu, Y.; Xiao, Q.; Hsieh, P.-L.; Wang, Y.; Li, F.; Quintero-Bermudez,

R.; Zhou, Y.; Chen, P.; Pang, Y.; Lo, S.-C.; Chen, L.-J.; Tan, H.; Xu, Z.; Zhao, S.; Sinton, D.; Sargent, E.H. Copper-on-Nitride Enhances the Stable Electrosynthesis of Multi-Carbon Products from CO_2. *Nat. Commun.* **2018**, *9*, 3828.

31.Luna, P.D.; Quintero-Bermudez, R.; Dinh, C.-T.; Ross, M.B.; Bushuyev, O.S.; Todorović, P.; Regier, T.; Kelley, S.O.; Yang, P.; Sargent, E.H. Catalyst Electro-Redeposition Controls Morphology and Oxidation State for Selective Carbon Dioxide Reduction. *Nat. Catal.* **2018**, *1*, 103-110.

32.Mistry, H.; Varela, A.S.; Bonifacio, C.S.; Zegkinoglou, I.; Sinev, I.; Choi, Y.-W.; Kisslinger, K.; Stach, E.A.; Yang, J.C.; Strasser, P.; Cuenya, B.R. Highly Selective Plasma-Activated Copper Catalysts for Carbon Dioxide Reduction to Ethylene. *Nat. Commun.* **2016**, *7*, 12123.

33.Ting, L.R.L.; Piqué, O.; Lim, S.Y.; Tanhaei, M.; Calle-Vallejo, F.; Yeo, B.S. Enhancing CO_2 Electroreduction to Ethanol on Copper–Silver Composites by Opening an Alternative Catalytic Pathway. *ACS Catal.* **2020**, *10*, 4059-4069.

34.Ren, D.; Ang, B.S.-H.; Yeo, B.S. Tuning the Selectivity of Carbon Dioxide Electroreduction toward Ethanol on Oxide-Derived Cu_xZn Catalysts. *ACS Catal.* **2016**, *6*, 8239-8247.

35.Morales-Guio, C.G.; Cave, E.R.; Nitopi, S.A.; Feaster, J.T.; Wang, L.; Kuhl, K.P.; Jackson, A.; Johnson, N. C.; Abram, D.N.; Hatsukade, T.; Hahn, C.; Jaramillo, T.F. Improved CO_2 Reduction Activity towards C_{2+} Alcohols on a Tandem Gold on Copper Electrocatalyst. *Nat. Catal.* **2018**, *1*, 764-771.

36.Li, F.; Li, Y.C.;Wang, Z.; Li, J.; Nam, D.-H.; Lum, Y.; Luo, M.; Wang, X.; Ozden, A.; Hung, S.-F.; Chen, B.; Wang, Y.; Wicks, J.; Xu, Y.; Li, Y.; Gabardo, C.M.; Dinh, C.-T.; Wang, Y.; Zhuang, T.-T.; Sinton, D.; Sargent, E.H. Cooperative CO_2-to-Ethanol Conversion via Enriched Intermediates at Molecule–Metal Catalyst Interfaces. *Nat. Catal.* **2020**, *3*, 75-82.

37.Montoya, J.H.; Shi, C.; Chan, K.; Nørskov, J.K. Theoretical Insights into A CO Dimerization Mechanism in CO_2 Electroreduction. *J. Phys. Chem. Lett.* **2015**, *6*, 2032-2037.

38.Vasileff, A.; Xu, C.; Jiao, Y.; Zheng, Y.; Qiao, S.-Z. Surface and Interface Engineering in Copper-Based Bimetallic Materials for Selective CO_2 Electroreduction. *Chem* **2018**, *4*, 1809-1831.

39.Liu, K.; Ma, M.; Wu, L.; Valenti, M.; Cardenas-Morcoso, D.; Hofmann, J.P.; Bisquert, J.; Gimenez, S.; Smith, W.A. Electronic Effects Determine the Selectivity of Planar Au–Cu Bimetallic Thin Films for Electrochemical CO_2 Reduction. *ACS Appl. Mater. & Interfaces* **2019**, *11*, 16546-16555.

40.Kim, D.; Resasco, J.; Yu, Y.; Asiri A.M.; Yang, P. Synergistic Geometric and Electronic Effects for Electrochemical Reduction of Carbon Dioxide Using Gold–Copper Bimetallic Nanoparticles. *Nat. Commun.* **2014**, *5*, 4948.

41.Huang, J.; Mensi, M.; Oveisi, E.; Mantella, V.; Buonsanti, R. Structural Sensitivities in Bimetallic Catalysts for Electrochemical CO_2 Reduction Revealed by Ag–Cu Nanodimers. *J. Am. Chem. Soc.* **2019**, *141*, 2490-2499.

42.Jeon, H.S.; Timoshenko, J.; Scholten, F.; Sinev, I.; Herzog, A.; Haase, F.T.; Cuenya, B.R. *Operando* Insight into the Correlation between the Structure and Composition of CuZn Nanoparticles and their Selectivity for the Electrochemical CO_2 Reduction. *J. Am. Chem. Soc.* **2019**, *141*, 19879-19887.

43.Eren, B.; Zherebetskyy, D.; Patera, L.L.; Wu, C.H.; Bluhm, H.; Africh, C.; Wang, L.W.; Somorjai, G.A.; Salmeron, M. Activation of Cu (111) Surface by Decomposition into Nanoclusters Driven by CO Adsorption. *Science* **2016**, *351*, 475-478.

44.Kim, Y.-G.; Baricuatro, J.H.; Javier, A.; Gregoire, J.M.; Soriaga, M.P.The Evolution of the Polycrystalline Copper Surface, First to Cu (111) and then to Cu (100), at A Fixed CO_2RR Potential: A study by *Operando* EC-STM. *Langmuir* **2014**, *30*, 15053-15056.

45.Wang, X.; Araújo, J.F.; Ju, W.; Bagger, A.; Schmies, H.; Kühl, S.; Rossmeisl, J.; Strasser, P. Mechanistic eaction paPthways of Enhanced Ethylene Yields during Electroreduction of CO

2–CO Co-Feeds on Cu and Cu-Tandem Electrocatalysts. *Nat. Nanotechnol*, **2019**, *14*, 1063-1070.

46. Luna, P.D.; Hahn, C.; Higgins, D.; Jaffer, S.A.; Jaramillo, T.; Sargent, E.H., What Would it Take for Renewably Powered Electrosynthesis to Displace Petrochemical rocesses? *Science* **2019**, *364*, eaav3506.

47. Jouny, M.; Hutchings, G.S.; Jiao, F. Carbon mMonoxide Electroreduction as An Emerging Platform for Carbon Utilization. *Nat. Catal. 2019*, *2*, 1062-1070.

48. Huan, T.N.; Ranjbar, N.; Rousse, G.; Sougrati, M.; Zitolo, A.; Mougel, V.; Jaouen, F.; Fontecave, M. Electrochemical Reduction of CO_2 Catalyzed by Fe-NC Materials: A Structure–Selectivity Study. *ACS Catal.* **2017**, *7*, 1520-1525.

49. Fan, X.; Peng, Z.; Ye, R.; Zhou, H.; Guo, X. M_3C (M: Fe, Co, Ni) Nanocrystals Encased in Graphene Nanoribbons: An Active and Stable Bifunctional Electrocatalyst for Oxygen Reduction and Hydrogen Evolution Reactions. *ACS Nano* **2015**, *9*, 7407-7418.

50. Jin, Q.; Ren, B.; Li, D.; Cui, H.; Wang, C. In Situ Promoting Water Dissociation Kinetic of Co Based Electrocatalyst for Unprecedentedly Enhanced Hydrogen Evolution Reaction in Alkaline Media. *Nano Energy* **2018**, *49*, 14-22.

51. Zhao, C.; Dai, X.; Yao, T.; Chen, W.; Wang, X.; Wang, J.; Yang, J.; Wei, S.; Wu, Y.; Li, Y. Ionic Exchange of Metal–Organic Frameworks to Access Single Nickel Sites for Efficient Electroreduction of CO_2. *J. Am. Chem. Soc.* **2017**, *139*, 8078-8081.

52. Ren, S.; Joulié, D.; Salvatore, D.; Torbensen, K.; Wang, M.; Robert, M.; Berlinguette, C.P. Molecular Electrocatalysts Can Mediate Fast, Selective CO_2 Reduction in A Flow Cell. *Science* **2019**, *365*, 367-369.

53. Zhang, Z.; Xiao, J.; Chen, X.-J.; Yu, S.; Yu, L.; Si, R.; Wang, Y.; Wang, S.; Meng, X.; Wang, Y.; Tian, Z.-Q.; Deng, D. Reaction Mechanisms of Well‐Defined Metal–N_4 Sites in Electrocatalytic CO_2 Reduction. *Angew. Chem. Int. Ed.* **2018**, *57*, 16339-16342.

54. Costentin, C.; Drouet, S.; Robert, M.; Savéant, J.-M. A Local Proton Source Enhances CO_2 Electroreduction to CO by A Molecular Fe Catalyst. *Science* **2012**, *338*, 90-94.

55. Karapinar, D.; Huan, N.T.; Sahraie, N.R.; Li, J.; Wakerley, D.; Touati, N.; Zanna, S.; Taverna, D.; Tizei, L.H.G.; Zitolo, A.; Jaouen, F.; Mougel, V.; Fontecave, M. Electroreduction of CO_2 on Single‐Site Copper‐Nitrogen‐Doped Carbon Material: Selective Formation of Ethanol and Reversible Restructuration of the Metal Sites. *Angew. Chem. Int. Ed.* **2019**, *58*, 15098-15103.

56. Weng, Z.; Wu, Y.; Wang, M.; Jiang, J.; Yang, K.; Huo, S.; Wang, X.-F.; Ma, Q.; Brudvig, G.W.; Batista, V.S.; Liang, Y.; Feng, Z.; Wang, H. Active Sites of Copper-Complex Catalytic Materials for Electrochemical Carbon Dioxide Reduction. *Nat. Commun.* **2018**, *9*, 415.

57. Jaouen, F. Heat‐Treated Transition Metal‐N_xC_y Electrocatalysts for the O_2 Reduction Reaction in Acid PEM Fuel Cells. In *Non‐Noble Metal Fuel Cell Catalysts*; Wiley‐VCH Verlag GmbH & Co. KGaA, **2014**, 29-118.

58. Mineva, T.; Matanovic, I.; Atanassov, P.; Sougrati, M.-T.; Stievano, L.; Clémancey, M.; Kochem, A.; Latour, J.-M.; Jaouen, F. Understanding Active Sites in Pyrolyzed Fe–N–C Catalysts for Fuel Cell Cathodes by Bridging Density Functional Theory Calculations and [57]Fe Mössbauer Spectroscopy. *ACS Catal.* **2019**, *9*, 9359-9371.

59. Sougrati, M.T.; Goellner, V.; Schuppert, A.K.; Stievano, L.; Jaouen, F. Probing Active Sites in Iron-Based Catalysts for Oxygen Electro-Reduction: A Temperature-Dependent [57]Fe Mössbauer Spectroscopy Study. *Catal. Today*, **2016**, *262*, 110-120.

60. Menga, D.; Ruiz-Zepeda, F.; Moriau, L.; Šala, M.; Wagner, F.; Koyutürk, B.; Bele, M.; Petek, U.; Hodnik, N.; Gaberšček, M.; Fellinger, T.-P. Active-Site Imprinting: Preparation of Fe–N–C Catalysts from Zinc Ion–Templated Ionothermal Nitrogen‐Doped Carbons. *Adv. Energy Mater.* **2019**, *9*, 1902412.

61.Mehmood, A.; Pampel, J.; Ali, G.; Ha, H.Y.; Ruiz-Zepeda, F.; Fellinger, T.-P. Facile Metal Coordination of Active Site Imprinted Nitrogen Doped Carbons for the Conservative Preparation of Non-Noble Metal Oxygen Reduction Electrocatalysts. *Adv. Energy Mater.* **2018**, *8*, 1701771.

62.Kamali-M, S.; Ericsson, T.; Wäppling, R. Characterization of Iron Oxide Nanoparticles by Mössbauer Spectroscopy. *Thin Solid Films* **2006**, *515*, 721-723.

63. Li, J.; Sougrati, M.T.; Zitolo, A.; Ablett, J.M.; Oğuz, I.C.; Mineva, T.; Matanovic, I.; Atanassov, P.; Huang, Y.; Zenyuk, I.; Cicco, A.D.; Kumar, K.; Dubau, L.; Maillard, F.; Dražić, G.; Jaouen, F. Identification of durable and non-durable FeN_x sites in Fe–N–C materials for proton exchange membrane fuel cells. *Nat. Catal.* **2021**, *4*, 10-19.

64.Zboril, R.; Mashlan, M.; Petridis, D. Iron (III) Oxides from Thermal Processes Synthesis, tructural and Magnetic Properties, Mössbauer Spectroscopy Characterization, and Applications. *Chem. Mater.* **2002**, *14*, 969-982.

65.Fultz, B. Mössbauer spectrometry. In *Characterization of materials*, Wiley‑VCH Verlag GmbH & Co. KGaA, **2002**, 1-21.

66. Li, J.; Ghoshal, S.; Liang, W.; Sougrati, M.-T.; Jaouen, F.; Halevi, B.; McKinney, S.; McCool, G.; Ma, C.; Yuan, X. J.; Ma, Z.-F.; Mukerjee, S.; Jia, Q. Structural and Mechanistic Basis for the High Activity of Fe−N−C Catalysts toward Oxygen Reduction. *Energy Environ. Sci.* **2016**, *9*, 2418−2432.

67. Zitolo, A.; Goellner, V.; Armel, V.; Sougrati, M.-T.; Mineva, T.; Stievano, L.; Fonda, E.; Jaouen, F. Identification of Catalytic Sites for Oxygen Reduction in Iron-and Nitrogen-Doped Graphene Materials. *Nat. Mater.* **2015**, *14*, 937-942.

68.Hötger, D.; Abufager, P.; Morchutt, C.; Alexa, P.; Grumelli, D.; Dreiser, J.; Stepanow, S.; Gambardella, P.; Busnengo, H.F.; Etzkorn, M.; Gutzler, R.; Kern, K. On-Surface Transmetalation of Metalloporphyrins. *Nanoscale* **2018**, *10*, 21116-21122.

69.Lee, J.A.; Newnham, C.E.; Stone, F.S.; Tye, F.L. Thermal Decomposition of Managanese Oxyhydroxide. *J. Solid State Chem.* **1980**, *31*, 81-93.

70.Li, Y.; Liu, L.-D.; Liu, L.; Liu, Y.; Zhang, H.-W.; Han, X. Efficient Oxidation of Phenol by Persulfate Using Manganite as A Catalyst. *J. Mol. Catal. A: Chem.* **2016**, *411*, 264-271.

71.Hyun, G.; Song, J.T.; Ahn, C.; Ham, Y.; Cho, D.; Oh, J.; Jeon, S. Hierarchically Porous Au Nanostructures with Interconnected Channels for Efficient Mass Transport in Electrocatalytic CO_2 Reduction. *Proc. Natl. Acad. Sci. U.S.A* **2020**, *117*, 5680-5685.

72.He, Q.; Lee, J.H.; Liu, D.; Liu, Y.; Lin, Z.; Xie, Z.; Hwang, S.; Kattel, S.; Song, L.; Chen, J.G. Accelerating CO_2 Electroreduction to CO Over Pd Single‑Atom Catalyst. *Adv. Funct. Mater.* **2020**, *30*, 2000407.

73.Asset, T.; Garcia, S.T.; Herrera, S.; Andersen, N.; Chen, Y.; Peterson, E.J.; Matanovic, I.; Artyushkova, K.; Lee, J.; Minteer, S.D.; Dai, S.; Pan, X.; Chavan, K.; Barton, S.C.; Atanassov, P. Investigating the Nature of the Active Sites for the CO_2 Reduction Reaction on Carbon-Based Electrocatalysts. *ACS Catal.* **2019**, *9*, 7668-7678.

74.Handoko, A.D.; Wei, F.; Jenndy, Yeo, B.S.; She, Z.W. Understanding Heterogeneous Electrocatalytic Carbon Dioxide Reduction through *Operando* Techniques. *Nat. Catal.* **2018**, *1*, 922-934.

75.Zhu, Y.; Wang, J.; Chu, H.; Chu, Y.-H.; Chen, H.M. *In Situ/Operando* Studies for Designing Next-generation Electrocatalysts. *ACS Energy Lett.* **2020**, *5*, 1281-1291.

76.Ma, L.; Hu, W.; Mei, B.; Liu, H.; Yuan, B.; Zang, J.; Chen, T.; Zou, L.; Zou, Z.; Yang, B.; Yu, Y.; Ma, J.; Jiang, Z.; Wen, K.; Yang, H. Covalent Triazine Framework Confined Copper Catalysts for Selective Electrochemical CO_2 Reduction: *Operando* Diagnosis of Active Sites. *ACS Catal.* **2020**, *8*, 4534-4542.

77.Nam, D.-H.; Bushuyev, O.S.; Li, J.; Luna, P.D.; Seifitokaldani, A.; Dinh, C.-T.; Arquer, F.P.G.; Wang, Y.; Liang, Z.; Proppe, A.H.; Tan, C.S.; Todorović, P.; Shekhah, O.; Gabardo,

C.M.; Jo, J.W.; Choi, J.; Choi, M.-J.; Baek, S.-W.; Kim, J.; Sinton, D.; Kelley, S.O.; Eddaoudi, M.; Sargent, E.H. Metal–Organic Frameworks Mediate Cu Coordination for Selective CO_2 Electroreduction. *J. Am. Chem. Soc.* **2018**, *140*, 11378-11386.

78. Möller, T.; Scholten, F.; Thanh, T.N.; Sinev, I.; Timoshenko, J.; Wang, X.L.; Jovanov, Z.; Gliech, M.; Cuenya, B.R.; Varela, A.S.; Strasser, P. Electrocatalytic CO_2 Reduction on CuO_x Nanocubes Tracking the Evolution of Chemical State, Geometric Structure, and Catalytic Selectivity using *Operando* Spectroscopy. *Angew. Chem. Int. Ed.* **2020**, *59*, 17974-17983.

79. Adak, S.; Hartl, M.; Daemen, L.; Fohtung, E.; Nakotte, H. Study of Oxidation States of the Transition Metals in a Series of Prussian Blue Analogs using X-Ray Absorption Near Edge Structure (XANES) Spectroscopy. *J. Electron Spectros. Relat. Phenomena* **2017**, *214*, 8-19.

80. Gardner, T.H.; Spivey, J.J.; Kugler, E.L.; Campos, A.; Hissam, J.C.; Roy, A.D. Structural Characterization of Ni-Substituted Hexaaluminate Catalysts using EXAFS, XANES, XPS, XRD, and TPR. *J. Phys. Chem. C* **2010**, 114, 7888-7894.

81. Friebel, D.; Louie, M.W.; Bajdich, M.; Sanwald, K.E.; Cai, Y.; Wise, A.M.; Cheng, M.-J.; Sokaras, D.; Weng, T.-S.; Alonso-Mori, R.; Davis, R.C.; Bargar, J.R.; Nørskov, J.K.; Nilsson, A.; Bell, A.T. Identification of Highly Active Fe Sites in (Ni, Fe)OOH for Electrocatalytic Water Splitting. *J. Am. Chem. Soc.* **2015**, *140*, 1305-1313.

82. Jiang, J.; Sun, F.; Zhou, S.; Hu, W.; Zhang, H.; Dong, J.; Jiang, Z.; Zhao, J.; Li, J.; Yan, W.; Wang, M. Atomic-Level Insight into Super-Efficient Electrocatalytic Oxygen Evolution on Iron and Vanadium Co-Doped Nickel (oxy) ydroxide. *Nat. Commun.* **2018**, *9*, 2885.

83. Scheinost, A.C.; Sparks, D.L. Formation of Layered Single-and Double-Metal Hydroxide Precipitates at the Mineral/Water Interface: A Multiple-Scattering XAFS Analysis. *J. Colloid Interface Sci.* **2000**, *223*, 167-178.

84. Hall, D.S.; Lockwood, D.J.; Bock, C.; MacDougall, B.R. Nickel Hydroxides and Related Materials: A Review of Their Structures, Synthesis and Properties. *Proc. R. Soc. A* **2015**, *471*.

85. Chen, Y.; Bylaska, E.J.; Weare, J.H. Weakly Bound Water Structure, Bond Valence Saturation and Water Dynamics at the Goethite (100) Surface/Aqueous Interface: Ab Initio Dynamical Simulations. *Geochemical Trans.* **2017**, *18*, 3.

86. Ma, R.; Liu, Z.; Takada, K.; Fukuda, K.; Ebina, Y.; Bando, Y.; Sasaki, T.; Tetrahedral Co(II) Coordination in α-Type Cobalt Hydroxide: Rietveld Refinement and X-Ray Absorption Spectroscopy. *Inorg. Chem.* **2006**, *45*, 3964-3969.

87. Dunwell, M.; Lu, Q.; Heyes, J.M.; Rosen, J.; Chen, J.G.; Yan, Y.; Jiao, F.; Xu, B. The Central Role of Bicarbonate in the Electrochemical Reduction of Carbon Dioxide on Gold. *J. Am. Chem. Soc.* **2017**, *139*, 3774-3783.

88. Zhu, S.; Jiang, B.; Cai, W.-B.; Shao, M. Direct Observation on Reaction Intermediates and the Role of Bicarbonate Anions in CO_2 Electrochemical Reduction Reaction on Cu Surfaces. *J. Am. Chem. Soc.* **2017**, *139*, 15664-15667.

89. Bergmann, A.; Martinez-Moreno, E.; Teschner, D.; Chernev, P.; Gliech, M.; Araújo, J.F.; Reier, T.; Dau, H.; Strasser, P. Reversible Amorphization and the Catalytically Active State of Crystalline Co_3O_4 during Oxygen Evolution. *Nat. Commun.* **2015**, *6*, 8625.

90. Zhou, H.; Yu, F.; Sun, J.; He, R.; Chen, S.; Chu, C.-W.; Ren, Z. Highly Active Catalyst Derived from a 3D Foam of $Fe(PO_3)_2/Ni_2P$ for Extremely Efficient Water Oxidation. *Proc. Natl. Acad. Sci. U.S.A* **2017**, *114*, 5607-5611.
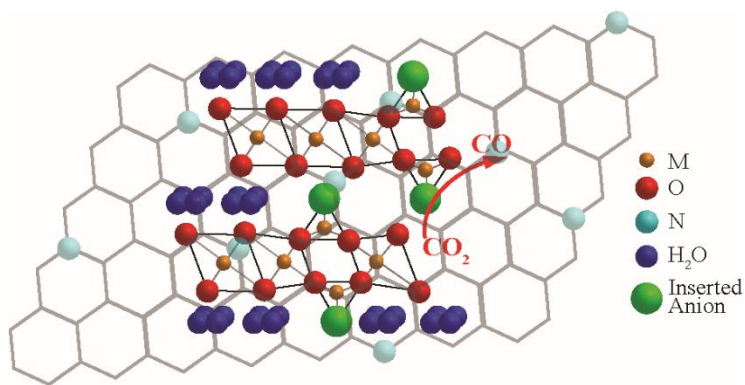
1
2
3
4
5
6
7
8
9
10
11
12
13
14
15
16
17
18
19
20
21
22
23
24
25
26
27
28
29
30
31
32
33
34
35
36
37
38
39
40
41
42
43
44
45
46
47
48
49
50
51
52
53
54
55
56
57
58
59
60

TOC